Design and Fabrication of Photonic Crystal Materials and Components

Harpøth, Anders; Kristensen, Martin

Publication date:
2005

Document Version
Publisher's PDF, also known as Version of record

Citation (APA):
Harpøth, A., & Kristensen, M. (2005). Design and Fabrication of Photonic Crystal Materials and Components.

Design and Fabrication of Photonic Crystal Materials and Components

Anders Harpøth

revised version:
Marts 2005

Research Center COM
Technical University of Denmark
Building 345V
2800 Kgs. Lyngby
DENMARK

Abstract

The work described in this thesis covers the issues of producing materials for use as base material for fabricating photonic crystals and the design, fabrication and characterization of photonic crystal components.

One of the aims is to investigate the possibilities of fabricating a silicon-on-insulator (SOI) material using standard cleanroom processing techniques. A standard silicon wafer is covered with a silica film by an oxidation process and subsequently covered with a thin silicon layer deposited from silane by a low pressure chemical vapor deposition (LPCVD) process. Such a process sequence is in principle rather straightforward and benefits from being much cheaper compared to acquiring commercially available SOI materials. Different issues as deposition temperature, surface roughness, crystallization, and silicon waveguide geometries have been investigated in order to reduce the optical loss in the deposited silicon films and to open for a potential use with photonic crystals.

In relation to photonic crystal structures, different properties have been investigated by using modeling tools such as the plane wave expansion method and the finite-difference time-domain method. Furthermore different approaches to improve the performance of selected components have been carried out by applying a method adopted from mechanical engineering called topology optimization. Also different approaches have been applied in order to investigate the loss of light when coupled to cavity resonators. Finally, the fabrication of several components has been carried out with a subsequent characterization of the fabricated components.

Sammendrag

Denne afhandling beskriver det arbejde der er blevet udført med henblik på at fremstille materialer til brug for fotoniske krystaller samt design, fabrikation og karakterisering af fotoniske krystalkomponenter.

Et af målene er at undersøge mulighederne for at fremstille en struktur bestående af et tyndt lag silicium adskilt fra et silicium-substrat af et tyndt lag silica ved at benytte standard renrumsteknikker. En standard silicium wafer dækkes af et tyndt lag silica ved en termisk oxideringsprocess. Derefter dækkes den med et tyndt lag silicium ved brug af en 'low pressure chemical vapor deposition' process. Denne processsekvens er forholdsvis simpel at udføre og har den fordel at de fremstillede strukturer vil være væsentligt billigere sammenlignet med at anskaffe dem kommercielt. Med henblik på potentiel brug til fremstilling af fotoniske krystalkomponenter er forskellige undersøgelser, for at reducere udbredelsestabet i det deponerede silicium-lag, blevet udført. Dette omfatter undersøgelser af deponeringstemperatur, overfladeruhed, krystallisering og forskellige geometrier for bølgeledere.

Arbejdet med fotoniske krystaller har omfattet 'plane wave expansion' og 'finite-difference time-domain' simuleringer af de optiske egenskaber. Desuden er der brugt forskellige metoder til at optimere disse egenskaber for udvalgte typer komponenter. Her er blandt andet brugt en metode kaldet 'topologi optimering', som stammer fra design af mekaniske strukturer, samt nogle undersøgelser af tabet af lys ved kobling til optiske kaviteter. Desuden er adskillelige af de undersøgte komponenter blevet fabrikeret og den endelige optiske karakterisering er blevet foretaget.

Preface

The work presented in this thesis was carried out in the Poling and Grating group at Research Center COM under supervision of Professor Martin Kristensen, who I would like to give my most sincere thanks for giving me this opportunity to work in his research group and his help throughout the project.

Many people have provided a lot of help, for which I am very grateful. These include Lars Pleth Nielsen and Britt Hvolbæk Larsen for introducing me to all the necessary equipment in the cleanroom. Peixiong Shi for giving me the opportunity to make a few runs on the e-beam machine before it was stored away for a long time. Jakob Jensen and Ole Sigmund for supplying some very nice designs. Lars Hagedorn Frandsen and Peter Ingo Borel for good daily cooperation working with a truly amazing research field and also to make life less miserable through frustrating times. The last point is also directed to Rasmus Kousholt Sandbjerg, Henrik Rokjær Sørensen, Jacob Fage Pedersen, and 'fiberdrengene'. And of course my family and friends for support and encouragement.

Furthermore Peter Ingo Borel and Lars Hagedorn Frandsen are also thanked for their great help by proofreading my thesis.

Contents

Chapter 1

Introduction

The optical telecommunication technologies have matured significantly during the last decade. Today, the most common and mature commercial technologies are based on silica-on-silicon materials. Optical waveguides made in such materials suffer from large bending radii, and thereby a large size of the integrated optical components, due to a low index contrast between the waveguide core and the cladding layer. Within optical telecommunication there is an increasingly demand for decreasing the size of the components in order to increase the device packing density, and hence to reduce the fabrication cost. The minimum bending radius can be reduced markedly by increasing the refractive index contrast. Due to improved fabrication technologies high quality silicon-on-insulator (SOI) can be achieved [1] and such material has emerged as a potential platform for photonics. SOI is an attractive platform, not only due to a high index contrast and hence allows for miniaturization of the waveguide components, but it is also the material of choice for high performance complementary metal oxide semiconductor (CMOS) integrated circuits [2]. This opens for a potential hybrid integration of electronic and photonic circuits.

Photonic crystals were proposed in 1987 [3, 4], and are artificial materials with a periodic modulation of the refractive index. This leads to a photonic bandgap, wherein no light can propagate, and this way they provide great control of light on a sub-wavelength scale. Therefore they have draught a lot of scientific attention in connection with integrated optical components operating at the telecommunications wavelength [5] as their optical properties allow for the size of optical components and hence the fabrication cost to be greatly reduced. In principle a 3D photonic bandgap is needed in order to have complete control of the light propagation, but such structures are complicated to fabricate. Planar photonic crystals fabricated in a high index-contrast slab have shown to be a very promising candidate for realizing ultra-compact optical components [6]. Light is

confined by a combination of an in-plane photonic bandgap and total internal reflection in the out-of-plane direction. The propagation loss in photonic crystal components has been lowered considerably to ∼2.4 dB/cm [7], thereby opening up for the possibility for a practical implementation of such structures. The research is now heading to more complicated functionalities, and optical signal processing devices [8], dispersion compensators, transmission filters [9], multiple drop filters [10], and cavities with very high Q-values [11, 12] have been demonstrated. Planar photonic crystal structures only support leakage free guiding in a small fraction of the available bandwidth of the bandgap. Recently there have been an interest in using inverse design techniques in order to optimize bandwidth utilization for leakage free guidance [13]. This is a truly amazing research field [14] and a lot of activity is continuously being focussed on a further utilization of the unique optical properties provided by photonic crystal structures.

The goal of this project was to develop a SOI material using conventional cleanroom processes, and subsequently design and fabricate photonic crystal components in such material. The thesis is divided into six chapters, where **chapter 1** is this introduction. In **chapter 2** there is a description of the work done on fabricating a silicon-on-insulator structure by oxidation of a standard silicon wafer followed by low pressure chemical vapor deposition (LPCVD) of silicon by silane. This is an alternative method of achieving a silicon-on-insulator structure. The remaining chapters deal with different aspects of the work performed on photonic crystals. The basic theory and the used theoretical tools for numerically simulating the optical properties of photonic crystals are introduced in **chapter 3**. The plane wave expansion method is used to calculate the dispersion relation of the photonic crystal structures, and the finite-difference time-domain method is used to simulate the light propagation in the structure. Methods to optimize the performance of a given type of components is dealt with in **chapter 4** where different design methods have been applied for selected photonic crystal components. The final test is of course to realize the designed structures. The fabrication procedure includes e-beam lithography and reactive ion etch (RIE) to transfer the patterns into the substrate. These matters are described in **chapter 5** together with the final characterization procedure of the fabricated components, followed by a discussion of the obtained results. Finally, **chapter 6** contains the conclusion of the thesis.

The work presented in this thesis is to some extend done as a group effort and also in collaboration with other research departments. The work on fabricating the SOI materials is carried out solely by the author, whereas the work on photonic crystal fabrication was done as a part of the photonic crystal group at Research Center COM. In general, the plane wave expansion and finite-difference time-domain simulations of photonic crystal structures are done individually.

The topology optimization is performed by the Department of Mechanical Engineering, where the author initiated and participated in the preliminary work done on the add-drop filter.

Chapter 2

Materials

In optical telecommunication most integrated components are made of silica where the high index core is created by using different kinds of dopants, resulting in an index contrast between the cladding and the waveguide core of around $\Delta n = n_{\mathrm{core}} - n_{\mathrm{cladding}} \sim 10^{-3}$. Because of the low index contrast it is necessary with rather large bend radii in order to maintain a sufficiently low bending loss. In the prospect of future high densification of integrated optical circuits it is necessary to have smaller bend radii, which for instance can be achieved by increasing the refractive index contrast. A material that fulfils this criteria is bulk mono-crystalline silicon which has a refractive index $n_{\mathrm{Si}} \simeq 3.46$ at $\lambda = 1550$ nm compared to that of silica $n_{\mathrm{SiO_2}} \simeq 1.45$. Silicon is widely used in the electronics industry and it is possible to exploit known processing technologies using the CMOS fabrication line. Another important feature when using silicon is that it opens up for the possibility to make photonic band gap materials, which have draught a lot of scientific attention in connection with integrated optical components [15]. A more detailed discussion of photonic band gap materials is given in the subsequent chapters.

2.1 Silicon-on-insulator

Waveguiding in a thin silicon layer was first observed in 1978 leading to the suggestion of making devices with simultaneous integration of electrical and optical functions [16]. Several waveguiding structures using silicon have been proposed [17, 18]. Especially waveguiding in silicon-on-insulator (SOI) structures has been investigated [19–21]. A SOI structure consist of a film of mono-crystalline silicon separated from the bulk silicon substrate by a layer of silica (SiO_2). Mono-crystalline silicon is almost transparent at the wavelengths used for optical telecommunication and this kind of structure has emerged as a potential material for realizing high index contrast strip waveguides. The benchmark of achieving a propagation loss of <1.0 dB/cm was reached for waveguides with sub-micron dimensions in 2001 [22]. Furthermore it is expected that the propagations loss can be reduced down to 0.1 dB/cm [23]. This fact opened up for a potential use as interconnects by using the same fabrication technology as the electronics industry.

However, the fact that the top silicon layer must be mono-crystalline, but separated by an amorphous insulating layer from the mono-crystalline substrate poses a major difficulty in a fabrication procedure, as there is no deposition method that would result in a mono-crystalline film grown without some kind of crystal template below it [1].

2.1.1 Fabrication methods

The SOI fabrication technology is becoming increasingly common, but the stringent demands on the quality and thin thickness of the mono-crystalline structure make them significantly more difficult to produce than standard bulk silicon wafers. Three different main technologies have been widely used in obtaining such structures, as briefly described in the following. A review of the fabrication methods can be found in [1].

SIMOX

Separation by implantation of oxygen (SIMOX) is a fabrication technology where oxygen ions are implanted in a bulk silicon wafer which is subsequently annealed. The oxygen ions are implanted at an energy up to 200 keV which determines the thickness and depth of the SiO_2 layer. The dose should be as high as $>10^{18}$ cm^{-2} (two orders of magnitude higher than doses typically used in device fabrication) in order to achieve saturation at the stoichiometric concentration of SiO_2. The drawback of the high dose is severe damage of the as-implanted silicon. But through process optimization improved SOI substrates have been produced. The thickness of the buried silica layer can not be changed significantly due to the fabrication process. The upper silicon layer can subsequently be made thicker by epitaxial growth.

BESOI

Bonded and etched back silicon on insulator (BESOI) are fabricated by bonding two thermally oxidized bulk silicon wafers together and thinning down one them to the desired film thickness. As opposed to the SIMOX process, the film can potentially keep its bulk properties. It is very difficult to obtain very thin film layer from thinning down a 0.5–1.0 mm thick silicon wafer in order to produce uniform films in the 1000 Å range. However through substantial work a process[1] using plasma assisted chemical etching (PACE) has been developed. With this process wafers can be thinned down to 1000 Å ± 100 Å [24].

Smart-Cut and Unibond

Smart-Cut and Unibond uses both implantation and bonding. In this process protons are implanted into a thermally oxidized wafer, which is then bonded to another wafer. In the smart-cut process the implanted protons will act as a micro scalpel. A heating of the bonded wafers will cause a cleavage of the implanted silicon wafer at a very well defined penetration depth along the plane of the implanted protons. This process was patented in 1994 and in 1999 the French company SOITEC[2] started a production line for SOI-wafers based on this method.

Because of the expenses and difficulties in making SOI-materials by the above mentioned methods and because only a limited flexibility in the layer thicknesses can be obtained [25], there is a great interest in finding alternative methods for achieving materials/structures with similar optical properties. In part of this work the focus is on fabricating and investigating a silicon-on-insulator structure where the top silicon layer is formed from low pressure chemical vapor deposition (LPCVD) of silane gas (SiH_4).

Silicon formed by LPCVD of silane has been overlooked as a possible material for optical waveguides, since it has been reported to greatly absorb at the optical telecommunication wavelengths $\sim$1.3 μm and $\sim$1.5 μm [26, 27]. Scattering due to surface imperfections and grain boundaries are thought to provide these limitations in its usefulness. Therefore LPCVD silicon has been considered as a less desirable material for waveguiding compared to mono-crystalline silicon [17]. However systematic investigations have been carried out to address these issues further and have resulted in significant improvement of the loss characteristics of LPCVD silicon, as described in [25, 28–30]. A more detailed discussion will be presented in the following.

2.2 Deposition

The formation of a silicon layer by deposition of gaseous SiH_4 is a conceptional straightforward fabrication method, as the silicon layer is simply built up on a chosen substrate by continuously adsorbing material from the gas phase molecules. In this work a 4” standard silicon wafer covered with a thin layer of silica, in the range 0.5–2.0 μm depending on the application, is used. Such standard

---

[1] The process is known as AcuThin

[2] http://www.soitec.com

wafers are widely used as the basic material in microelectronics and integrated optics. Mono-crystalline silicon can be fabricated with high quality using epitaxial growth techniques [2] and can be bought commercially at a relative low cost. The thin silica layer is formed by an oxidation process of the silicon wafer.

2.2.1 Oxidation

The oxidation of silicon is a way of obtaining a high-quality silica layer on top of a silicon surface in a controlled and repeatable manner. Silica (SiO_2) is widely used in the microelectronics industry as electrical insulator or masking layer against implant or diffusion of dopants into silicon. The standard single mode fibers and the integrated optics technologies used in optical telecommunication are based on the use of silica where the optical properties are tailored by introducing different dopant species in the silica glass.

A silicon surface is easily oxidized when exposed to an oxidizing agent, whereby a thin layer of silica is formed. The thermal oxidation process of silicon can be carried out using two kinds of oxidizing agents [2]:

$$\mathrm{Si(s)} + \mathrm{O_2} \rightarrow \mathrm{SiO_2(s)} \tag{2.1}$$

$$\mathrm{Si(s)} + 2\mathrm{H_2O} \rightarrow \mathrm{SiO_2(s)} + 2\mathrm{H_2} \tag{2.2}$$

these processes are referred to as dry and wet oxidation, respectively. The oxidation process proceeds by diffusion of the oxidizing species through the formed silica to the silicon surface where the oxidation process takes place. This way the silicon-silica interface moves into the silicon by incorporating oxygen into the silicon material. For longer oxidation times the reaction is limited by the diffusion through the oxide, which can be enhanced by increasing the temperature. Oxidation processes are therefore carried out at high temperatures in the range 750–1100°C [31]. A model of the reaction kinetics of the oxidation process is described in [2, 32].

In this work the oxidation was performed at atmospheric pressure in a horizontal diffusion tube, where the wafers are placed vertically in a slotted quartz-carrier (boat) containing up to 25 wafers. The silicon wafers are oxidized using a wet oxidation process at 1100°C for 9 hours. According to the model in [32] these oxidation conditions would result in a thickness of around $\sim$2.0 μm. The obtained silica layer had a thickness of $\sim$1.8 μm and a refractive index $n \simeq 1.458$ which was measured using a prism coupler operating at 632.8 nm. The rate of oxidation increases monotonically with the equilibrium concentration of the oxidizing species in the oxide. As molecular H_2O has a much higher (nearly three orders of magnitude) equilibrium concentration than O_2 in SiO_2, the oxidation rate is substantially higher when using a wet oxidation. If a dry oxidation process is used instead, it would take more than two days to obtain the same thickness.

For the purpose of guiding light it is necessary to have a sufficiently thick silica layer, separating the top silicon layer from the silicon substrate, to avoid the evanescent field of guided modes in the top silicon layer to couple to modes in the silicon substrate and thereby introduce leakage loss. In [20] a detailed theoretical study of penetration depth and coupling to the substrate for different modes was carried out. As expected the evanescent field extends further into the lower lying layers when the thickness of the upper silicon layer is decreased. For a silicon layer thickness of around ∼200–300 nm the silica should be at least ∼1 μm to have a coupling loss <0.01 dB/cm. Hence the obtained thickness of 1.8 μm of the oxide layer assures that the contribution from leakage loss to the substrate is negligible.

2.2.2 LPCVD

The deposition of silicon by SiH_4 is carried out using a low pressure chemical vapor deposition (LPCVD) process. Compared to atmospheric pressure, the low pressure deposition provides a higher deposition rate due to a higher absolute concentration of silane. It also provides a better control of the thickness uniformity since gas phase reactions leading to the formation of Si_2H_6 and possibly Si_3H_8 are reduced [33,34]. The flow dynamics in a low pressure system allow for closer positioning of the wafers, and the process has a potentially high throughput, with the capability of processing more than 100 wafers [35]. The used process chamber is a 3-zone resistively heated hot-wall quartz tube furnace [24]. The deposition process is usually performed by pyrolysis of silane at temperatures around 560–650°C, where decomposition of SiH_4 at the surface forms the silicon layer. The reaction is described by the following deposition steps:

$$\begin{aligned}
\mathrm{SiH_4(g)} &\leftrightharpoons \mathrm{SiH_4(ad)} \qquad (2.3)\\
\mathrm{SiH_4(ad)} &\leftrightharpoons \mathrm{SiH_2(ad)} + \mathrm{H_2(ad)} \qquad (2.4)\\
\mathrm{SiH_2(ad)} &\leftrightharpoons \mathrm{Si} + \mathrm{H_2(ad)} \qquad (2.5)\\
\mathrm{H_2(ad)} &\leftrightharpoons \mathrm{H_2(g)} \qquad (2.6)
\end{aligned}$$

The silicon deposition rate (R_{Si}) can be well described by the following expression [2]:

$$R_{\mathrm{Si}} = \frac{K_1 p_{\mathrm{SiH_4}}^{1/2}}{\left(1 + K_2 p_{\mathrm{SiH_4}}\right)^{1/2}} \qquad (2.7)$$

where $p_{\mathrm{SiH_4}}$ is the partial pressure of silane and K_1 and K_2 are derived from the equilibrium constants for the individual reaction steps. The process parameters are the temperature, the gas flow and the pressure in the reaction chamber. Figure 2.1 shows the experimentally obtained silicon thickness as a function of the partial pressure of Silane for three different deposition temperatures: $T =$

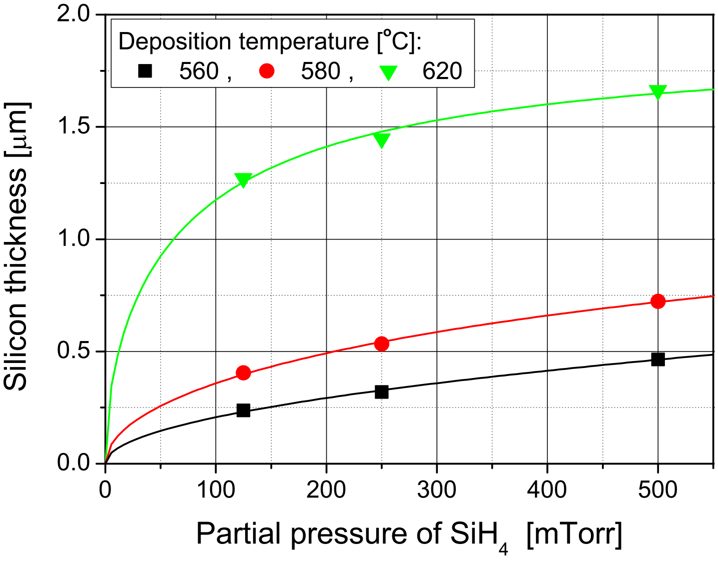

Figure 2.1: Thickness of the deposited silicon as a function of the partial pressure of silane in the reaction chamber, shown for three different deposition temperatures: $T = 560, 580, 620°\mathrm{C}$. The process time was 2 hours. The solid curves are obtained by fitting the data to equation (2.7).

$560, 580, 620°\mathrm{C}$. The process time was 2 hours. Also shown in the figure is the result of fitting the experimental data to the expression given in equation (2.7). The fitted curve is seen to have a good resemblance with the experimental values. It is also seen that the deposition rate increases as a function of temperature. The deposition rate for the different temperatures is estimated from figure 2.1 at a partial pressure of silane $p_{\mathrm{SiH}_4} = 250$ mTorr and is listed in table 2.1. The overall fabrication steps are illustrated in figure 2.2, and the three layered structures obtained this way are referred to as LPCVD SOI-substrates. Figure 2.3 shows a scanning electron microscope (SEM) image of a LPCVD SOI-substrate. The deposition process was carried out at $T = 560°\mathrm{C}$ for 1 hour and 52 min resulting in a ∼300 nm thick upper silicon layer.

Temperature (°C)	rate (nm/hour)
620	720
580	270
560	160

Table 2.1: The deposition rates of silane as a function of temperature at a partial pressure of silane $p_{\mathrm{SiH_4}} = 250$ mTorr

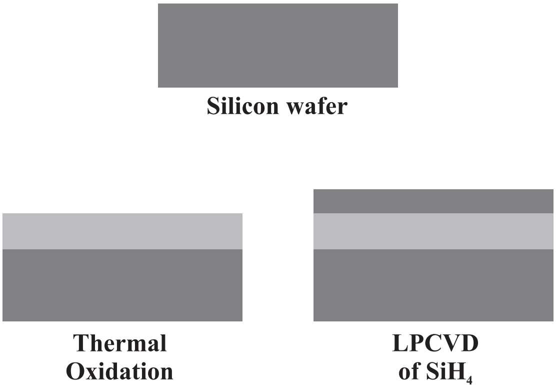

Figure 2.2: Schematic illustration of the fabrication steps used in the fabrication of a SOI-structure, including the oxidation of the silicon wafer followed by the LPCVD process.

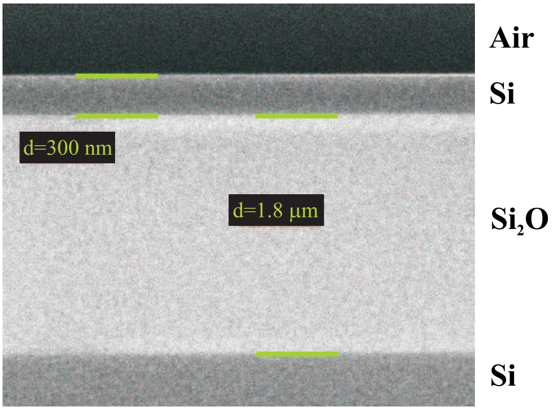

Figure 2.3: A SEM image of a fabricated three layered structure. The silica layer was formed by oxidation of a silicon wafer and the silicon layer by LPCVD of Silane. The oxide layer and the silicon layer have a thickness of ∼1.8 μm and ∼300 nm, respectively. The deposition temperature was 560°C.

2.2.3 Microstructure

In the LPCVD process the silane molecules are distributed randomly across the wafer during the deposition. As the buffer layer is amorphous silica no seeding for the crystal growth is possible. As a consequence different grains of silicon atoms will form on different locations on the substrate surface. Each grain will have a randomly distributed crystal orientation, which results in a layer that is poly-crystalline.

Poly-crystalline silicon

The poly-crystalline state is formed when the deposition temperature is above 600°C [2,36] in a low pressure system such as the one used in this work. In this situation the surface diffusion is sufficiently high so that clusters of atoms, the crystal grains, can be formed by nucleation [36].

Amorphous silicon

For temperatures below ∼600°C the surface diffusion, and thereby the nucleation rate, is lower reducing the grain formation. Furthermore the desorption rate of hydrogen is lower. In combination, this causes the hydrogen to occupy silicon dangling bonds and thereby preventing silicon in growing in crystal size.

Therefore the adsorbed hydrogen lead to vacancies and hence an amorphous Si structure as the hydrogen is buried under the growing surface [37].

To summarize, the incorporation of hydrogen in the structure has a great influence on whether the silicon becomes amorphous or poly-crystalline [37]. A more detailed description of the grain structure and texture can be found in [2, 36, 38]. The optical properties depend strongly on the microstructure of the formed silicon. State transitions have been reported in [39] to alter the optical properties, where the transition from the amorphous to the poly-crystalline state have been performed by annealing the silicon in nitrogen at temperatures >800°C, as will be described later.

2.3 Waveguides

The light propagation properties of the upper silicon layer of the LPCVD SOI-substrates are evaluated by making conventional straight strip waveguides in that layer and measuring their loss characteristics.

2.3.1 Waveguide fabrication

The waveguides are patterned on the LPCVD SOI-substrate using optical lithography, and a reactive ion etch (RIE) is used to transfer the waveguide patterns into the top silicon layer. As a final step some of the waveguide structures have been covered with a top cladding layer of silica using plasma enhanced chemical vapor deposition (PECVD). The fabrication steps are briefly described in the following.

Optical lithography

A very basic and important process in microfabrication is optical lithography, where a chosen substrate can be patterned according to a specific mask design. The substrate is covered with a UV sensitive photoresist by spin-coating. The resist is exposed through a transparent mask containing the opaque design pattern. Upon exposure the photoresist will undergo chemical transitions so that the exposed areas are removed and unexposed areas are left almost intact in a development process (positive resist type[3]). After development the remaining resist patterns are hardened by hot baking for 2 minutes at 120°C. The used lithographic process described above is a standard process and has not been subject to any optimization in this work. The mask used in this work is patterned with long straight waveguides with length $l = 8$ cm, almost extending a whole 4"-wafer, and widths $w = 4, 6, 8, 10$ μm. The resist thickness after

---

[3] for a negative resist type the unexposed areas are removed

the spin-coating, development and hard bake is ∼1.6 μm. The resist pattern now functions as masking material in an etching process where the pattern is transferred into the substrate.

Reactive ion etching

The etch was carried out using a reactive ion etch (RIE). The details on the etching process and etching parameters are described in section 5.1.2. The etching process can be monitored by end-point detection. This is done by measuring the intensity of a characteristic emission line of excited neutral atomic fluorine present in the plasma. The intensity of the characteristic emission line is proportional to the fluorine concentration, which depends strongly on the etching chemistry. The intensity is lower when the plasma is exposed to a silicon surface compared to a silica surface [40]. The silicon surface is initially covered with a thin native oxide layer and the end-point detected signal is high. The native oxide is quickly removed and the signal falls off to a lower value. The etching procedure is continued until the signal from the end-point detection reaches the initial level, indicating that the exposed silicon has been completely etched away, revealing the underlying silica layer.
The measured etching rate was almost the same for silicon deposited at 580°C and silicon deposited at 620°C and was measured to be 0.27 μm/min and 0.26 μm/min, respectively. The obtained resist thickness of ∼1.6 μm was sufficient for this purpose, as it was possible to etch waveguides with thicknesses up to 2 μm.

PECVD of silica

Some of the waveguides were covered with a cladding layer of silica using plasma enhanced chemical vapor deposition (PECVD) [35]. The process is carried out in a reaction chamber containing two horizontal plate electrodes opposing each other. The bottom electrode and the reaction chamber are connected to ground potential and the top electrode is connected to a 380 kHz RF-power generator operated at 380 W. The substrate is placed on the grounded electrode, which is heated to ∼300°C [24, 40]. The inlet gases are SiH_4 and N_2O, and the SiO_2 layer is formed by the net reaction:

$$\mathrm{SiH_4} + 2\mathrm{N_2O} \quad \longrightarrow \quad \mathrm{SiO_2} + 2\mathrm{N_2} + 2\mathrm{H_2} \tag{2.8}$$

The PECVD was performed using a standard process. The process parameters are listed in table 2.2.

A silica layer with a refractive index $n = 1.458$ and thickness $d \simeq 1$ μm was deposited. After deposition the samples were annealed for 4 hours at 1000°C to stabilize the glass. A scanning electron microscope (SEM) image of a waveguide

Parameter	Value	Unit
SiH_4 flow	17	sccm
N_2O flow	1600	sccm
Pressure	400	mTorr
Power	380	W
Temperature	300	°C

Table 2.2: The deposition parameters used in the PECVD process

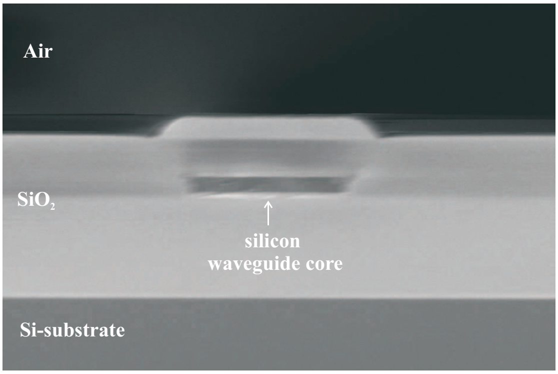

Figure 2.4: A SEM image of a waveguide core covered with PECVD glass

core covered with PECVD glass is shown in figure 2.4. The waveguide fabrication steps are sketched in figure 2.5.

2.3.2 Waveguide characterization

The quality of the silicon material is mainly characterized by the optical loss as a function of wavelength. The power loss of a lightwave propagating in the z-direction along an optical waveguide can in general be expressed as:

$$P(z) = P_0 \exp(-\alpha z) \tag{2.9}$$

where P_0 is the intensity at $z = 0$ and α is the attenuation coefficient. Experimentally the loss can be estimated using the cut-back method [31, 41], where the waveguide loss is measured for different waveguide lengths, z_1 and z_2:

$$\frac{P(z_1)}{P(z_2)} = \exp[-\alpha(z_1 - z_2)] \Rightarrow \alpha = \frac{\ln[P(z_1)/P(z_2)]}{z_1 - z_2} \tag{2.10}$$

and the propagation loss can be extracted by factoring out the coupling loss. The cut-back method is an easy and straightforward method to measure the

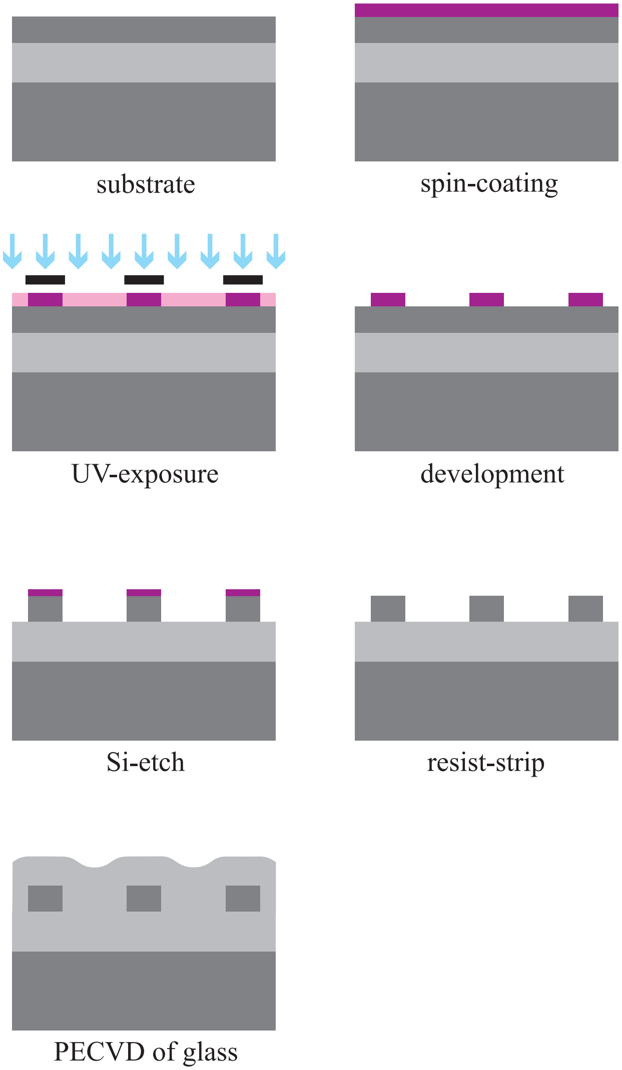

Figure 2.5: Illustration of the process steps of the fabrication for the silicon waveguides on SOI substrate.

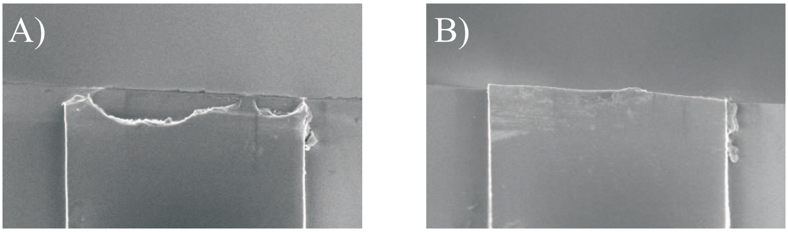

Figure 2.6: An SEM image of two end-facets of a cleaved waveguide viewed from above. A) a poor cleavage resulting in a lot of light scattering and thereby low coupling effiency, B) a good cleavage which will result in a much better coupling to the waveguide.

propagation loss. To access the waveguide core with a fiber, the wafer was cleaved into smaller pieces with lengths ranging from 4–20 mm. The fabricated waveguides have been characterized using the setup described in section 5.2.1. A tunable laser source was used to get a high input power $P \simeq 1$ mW at $\lambda = 1550$ nm. The light from the laser was butt-coupled in and out of the waveguides applying tapered lensed fibers. The output power is measured using an optical spectrum analyzer. Initially the goal was merely to get some light through the waveguides and they were characterized disregarding the polarization of the light.

A preliminary design goal was to achieve a waveguide structure where the upper silicon layer was either 500 nm or 2.0 μm. As the microstructure of the guiding material has a high influence on the optical properties, waveguides in both amorphous and poly-crystalline silicon layers were fabricated and characterized as described above.

A very important issue when coupling light from a fiber into the waveguides is the quality of the end-facets of the cleaved waveguides. Figure 2.6 shows two SEM images of end-facets of two cleaved waveguides. The end-facet in the left image of the figure is obviously not cleaved successfully and will cause severe scattering of the light and hence the coupling will be very inefficient. The end-facet in the right image is much more regular and from experience this will give a sufficiently good coupling efficiency. Generally it was possible to get good end-facets by cleaving the waveguides. From the preliminary characterization experiments it was at this point not possible to achieve high transmission through the waveguides. The shortest (4 mm) waveguides had an insertion loss of $\sim$65–70 dB, which is very high and not applicable for any practical purposes.

It was therefore necessary to make some more thorough investigations of both the fabricated LPCVD SOI-substrates and the waveguides.

2.4 Loss mechanisms

The structural and optical properties of the silicon layer formed by LPCVD deposition of silane are quite sensitive to the fabrication process parameters, and it is therefore necessary to make further investigations of these issues in order to optimize the optical properties of the final material.

The quality of the fabricated structures and materials for optical purposes is evaluated by estimating the optical loss in the thin deposited silicon films. Different loss mechanisms contribute to the total optical loss in the thin film waveguides. In this context it is obvious to make investigations of scattering losses from surface roughnesses, which has a great impact on the optical loss in the waveguides [25, 28, 29]. The edge of a waveguide is shown greatly magnified in figure 2.7 indicating that the roughness occurs from the fabrication process, both on the top-layer from the deposition process and on the sidewall from the etch process. In the following these loss mechanisms are briefly described and discussed.

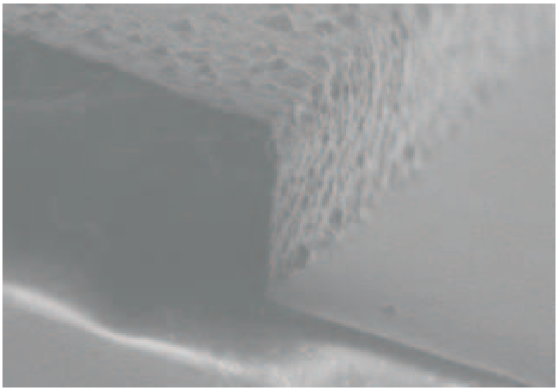

Figure 2.7: A SEM image of a cleaved waveguide, showing the roughness from both the deposition process (upper surface) and the etching process (edge to the right). The etching process is seen to be very anisotropic. It is also observed that the cleaved end-facet (edge to the left) is smooth. The silicon is deposited at 620°C and the thickness of the waveguide is 1.5 μm

Surface Roughness

The roughness resulting from the deposition process of the silicon layer has an important influence on the propagation loss, since it will cause scattering. The scattering loss occuring from the surface of the optical waveguides has been investigated theoretically by a number of authors. The models are rather complex and approximate methods are more attractive owing to their simplicity. Two models have been proposed, derived from the theoretical work reported in [42]. The model in [43] is based on the Rayleigh criterion relating the power in a beam incident on a surface to the power of the specular reflected beam. The model has been widely used as it provides a very simple analytic expression of the attenuation coefficient:

$$\alpha = A^2 \left(\frac{1}{2} \frac{\cos^3 \theta}{\sin \theta} \right) \left(\frac{1}{h + 1/p_1 + 1/p_2} \right) \tag{2.11}$$

where θ is the propagation angle within the waveguide, h is the height of the waveguide, p_1 and p_2 are the penetration depth of the guided mode into the upper and lower cladding, and A is given by:

$$A = \frac{4\pi n_1}{\lambda_0} \sqrt{(\sigma_1^2 + \sigma_2^2)} \tag{2.12}$$

where $\sigma_i, i = 1, 2$, is the root-mean-square (RMS)-roughness defined by:

$$\sigma_i \equiv \mathrm{RMS} = \sqrt{\frac{1}{N} \sum_{n=1}^{N} (z_n - \bar{z})^2} \tag{2.13}$$

and the subscript 1 and 2 refers to the upper and lower interfaces of the silicon layer, z_n is the height of the n'th sampling point and $\bar{z}$ is the mean height of all sampling points on the surface. This model is limited to long coherence lengths of the roughness profile [43] and for waveguide dimensions significantly larger than the wavelength of the light [31]. An improved model is derived in [44–47] where the coupling between guided and radiation modes caused by surface imperfections is included explicitly by use of a mathematical expression of the surface roughness. By assuming that the autocorrelation function of the surface roughness is exponential, as justified experimentally in [48], an analytic expression can be derived [31]:

$$\alpha = \varphi(d)^2 (\Delta n)^2 \left(\frac{k_0^2}{8 n_1} \right) \left(\frac{1}{n_{\mathrm{eff}} - n_2} \right) \sigma^2 \tag{2.14}$$

where Δn is the refractive index contrast between the waveguide core and the cladding, n_{eff} is the effective index of the mode, σ is the RMS-roughness of the interface and $\varphi(d)$ is the field intensity evaluated at the interface. The two methods are summarized and compared in [31]. No thorough theoretical investigations have been carried out in this work and the above expressions are merely used as qualitative guidelines. Both models state that the scattering is proportional to the RMS-roughness of the surface and it is evident that in order to reduce loss it is important to get a smooth surface. This has been investigated experimentally in [28] where the loss induced by roughness is compared to the measured loss change, indicating the importance of limiting the surface roughness. In [28] the authors also investigate the surface roughness of silicon films deposited at different temperatures. The surface of the fabricated films is characterized using an atomic force microscope (AFM) which measure the height profile across a surface on an atomic scale. From such measurements the RMS-roughness of the fabricated silicon films can be calculated using equation (2.13). AFM images of a silicon layer deposited at 620°C and 580°C are shown in figure 2.8 and 2.9. Note the different height scales.

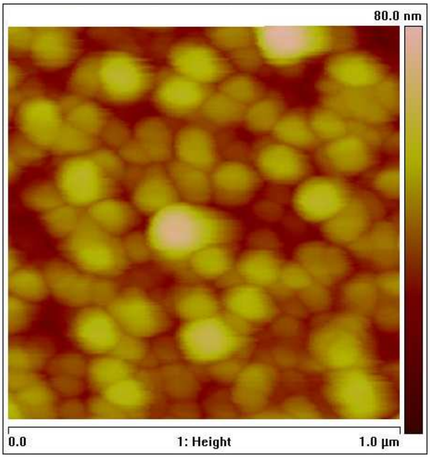

Figure 2.8: AFM image of a Si-film deposited at 620°C

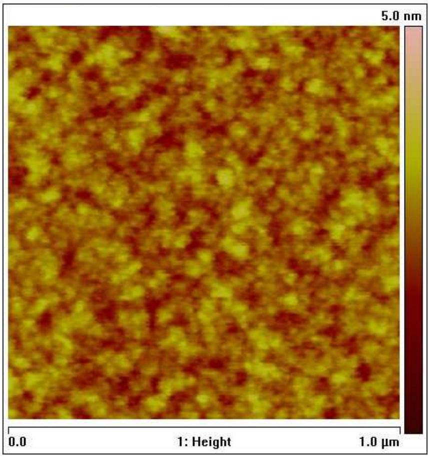

Figure 2.9: AFM image of a Si-film deposited at 580°C

The film deposited at 620°C show large variations in the roughness profile and large crystalline grains compared to the film deposited at 580°C. The corresponding RMS-roughness values are listed in table 2.3. Also listed is the value from silicon deposited at 560°C. It is seen that the RMS-roughness decreases with decreasing deposition temperature in agreement with [28]. The RMS-roughness is 8.1 nm when the silicon is deposited in the poly-crystalline state at a temperature of 620°C. The RMS-roughness is significantly decreased down to 0.41 nm if the silicon is deposited in its amorphous state at a temperature of 580°C. If the deposition temperature is further decreased down to 560°C the RMS-roughness only has an insignificant change from 0.41 nm to 0.33 nm. A 3D plot of the silicon surfaces deposited at 560°C and 580°C measured with the AFM is shown in figure 2.10.

Deposition Temperature	RMS (nm)
620°C	8.1
580°C	0.41
560°C	0.33

Table 2.3: The RMS-roughness of silicon deposited using LPCVD at different temperatures, obtained by AFM measurements

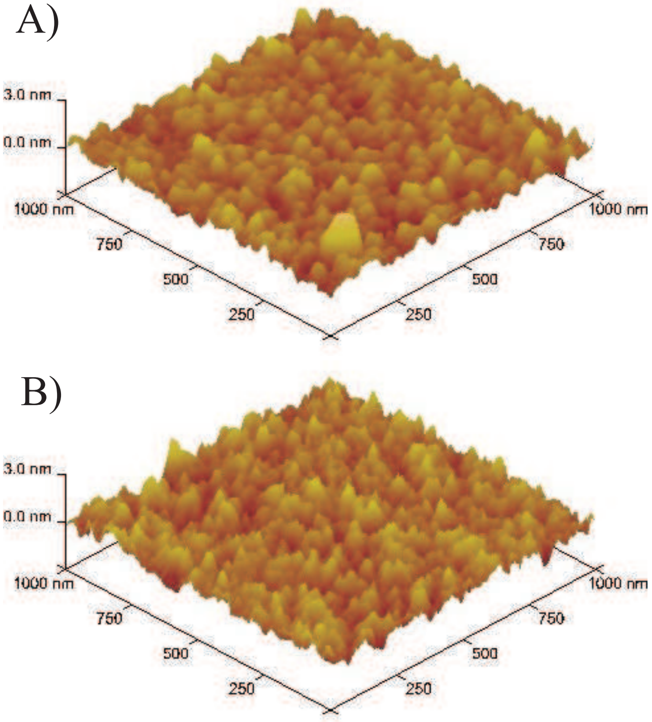

Figure 2.10: 3D AFM images of silicon deposited at: A) 560°C and B) 580°C

Substrate type	RMS (nm)
silicon wafer	< 0.10
oxidized wafer	0.14
SOI wafer	0.19

Table 2.4: AFM measurements showing the RMS-roughness of different substrates

Only a slightly more spiky behavior of the silicon deposited at 580°C is observed, and it is difficult to determine which one is best. Using equation (2.11) or equation (2.14) the loss difference for waveguides with RMS-roughness of 0.41 nm and 0.33 nm will be ∼0.3 dB/cm, which is practically unmeasurable.

According to the above discussion, a deposition at a temperature of 560°C gives the lowest RMS-roughness leading to a lower loss. The RMS-roughness measurements were all performed on silicon layers with a thickness of ∼300 nm.

In a previously reported study [49] it was observed that for a deposition temperature of 625°C the RMS-roughness increased from 1 nm to 25 nm when the thickness was increased from 200 nm to 1 μm. Therefore the RMS-roughness of a 2 μm thick layer deposited at a temperature of 560°C was measured. The measured RMS-roughness was 0.37 nm compared to 0.33 nm for a 300 nm thick layer. Hence changes in the surface scattering is found to be insignificant when increasing the thickness of the silicon layer at a deposition temperature of 560°C.

Roughness from oxidizing a silicon wafer is reported in [50] to initially increase as a function of time, but it converges to a RMS-roughness of ∼0.3 nm for a oxide thickness of ∼200 nm. This value is comparable to the measured RMS-roughness of the deposited silicon. To address the loss contributions from the different interfaces in the fabricated LPCVD SOI-structures, the RMS-roughness has been measured for an oxidized wafer. For comparison the RMS-roughness was also measured for a standard wafer and a commercial SOI-wafer fabricated by the Smart-cut and Unibond method, see section 2.1.1. The values are listed in table 2.4. It is seen that these values are small compared to the deposited silicon and are therefore negligible when considering losses from surface roughness.

The values of the RMS-roughness stated above are much lower than the ones reported elsewhere [25,28,29], where the samples have been annealed in order to (re)crystallize the silicon. In these cases the RMS-roughness ranged from 3.7–20.1 nm for the same deposition temperatures and silicon layer thicknesses. In the present work samples with a silicon layer deposited at 560°C were annealed at two different temperatures for 12 hours and the RMS-roughness increased to 5.6 nm and 9.8 nm for an annealing temperature of 800°C and 1100°C, respectively. The RMS-values are listed in table 2.5.

SEM images of a waveguide before and after annealing at 1100°C are shown

Anneal temperature	RMS (nm)
(no anneal)	0.33
800°C	5.6
1100°C	9.8

Table 2.5: AFM measurements showing the RMS-roughness of silicon deposited using LPCVD at 560°C and subsequently annealed for 12 hours.

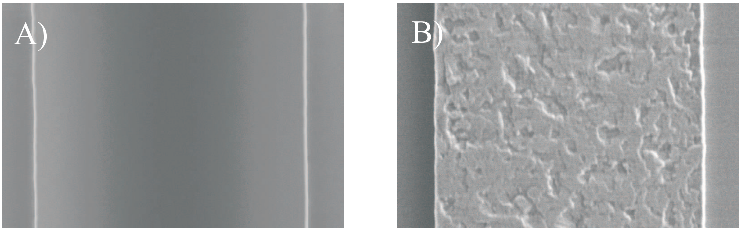

Figure 2.11: SEM images of a waveguide: A) before and B) after annealing at 1100°C

in figure 2.11 and the roughening of the surface which is caused by the crystallization and leads to grain formation is clearly seen.

Edge roughness

From the etching process some edge roughness of the sidewalls of the waveguides will appear, see figure 2.7. The waveguides are merely used as a tool for estimating the loss in the thin slab, and are not themselves the objective for these investigations. Fortunately scattering from the edge roughness can be made negligible if the waveguide core is made sufficiently wide. This is due to the fact that the modal field will be more confined to the waveguide core and the intensity of the field is smaller at the waveguide edge, whereby the scattered intensity is reduced according to equation (2.14).

This effect is studied in [23] where the authors investigate waveguides fabricated using a commercial SOI-structure, and the top and bottom surfaces are automatically very smooth due to the fabrication process. This way the surface scattering from the upper and lower surfaces can be ignored, and because the waveguides are characterized at a wavelength $\lambda = 1.54$ μm, where monocrystalline silicon have low absorption loss, the scattering analysis only takes into account scattering from the sidewall roughness. The propagation loss in a waveguide becomes almost negligible when a critical waveguide width of $\sim$4 μm is exceeded. In this paper the authors find good agreement between measured and calculated loss.

From these considerations the edge roughness of the waveguides fabricated in this work can be ignored, as the waveguides have widths up to 10 μm.

From waveguide characterization experiments the above mentioned behavior in such a high transmission loss is still observed in the waveguides. By comparing the results with the results reported in [28] the measured RMS-roughness of the fabricated samples cannot account for the very high loss. Hence, the remaining loss contributions may originate from scattering in the bulk of the silicon layers.

Bulk loss

In addition to losses caused by surface scattering, scattering will also occur in the bulk of the silicon. This scattering originates from imperfections in the bulk material, such as voids, contaminant atoms, or crystalline defects. Since the deposited silicon material does not form a mono-crystalline material, this is expected to have great importance. The microstructure is sensitive to fabrication parameters, see section 2.2.3, and it should be possible to control, to a certain extend, the optical properties of the bulk by applying or varying different fabrication steps.

A very thorough and careful investigation related to this subject has been carried out by others [30] as a continuation of the work described in [25, 29]. In these publications the authors investigate both the loss originating from surface and bulk scattering.

The amorphous state of silicon is reported to have a higher absorption loss compared to the poly-crystalline state, due to a higher concentration of defects caused by a higher hydrogen content, see section 2.2.3. The deposition in the amorphous state is necessary to get a smooth surface, but by a subsequent annealing, the amorphous state can be crystalized into the poly-crystalline state [25]. After an anneal process the size of the formed grains depends on the temperature used for the deposition. However it has been reported that the grain size have no significant influence on the loss in silicon films deposited between 560–625°C [25, 29].

In this work an annealing process has been performed on the fabricated structures with no measurable changes in the transmission loss of the waveguides. Also a low temperature anneal at 800°C followed by an anneal at 1100°C has been used. This approach was reported to reduce loss due to strain relief [30], but it did not result in any improvement in the propagation loss in the present study.

Geometrical loss

The modal field distribution depends on the geometry of the waveguide. If the waveguide core is made thicker, the field becomes more confined to the core and extends less into the surrounding cladding layer. The same picture applies when there is a higher index contrast. Having air as cladding will again make the field more confined in the waveguide core, but according to equation (2.14) a higher index contrast will increase the scattering.

On the other hand, if the field is less confined the field intensity at the interface between the core and the cladding is increased. As seen from equation (2.14) this will cause increased interface scattering, but in this case the field will also have a less overlap with the lossy waveguide core.

It is very difficult to make a firm conclusion based on the above considerations. Therefore various waveguide thicknesses of 300 nm and 2.0 μm combined with covering the waveguides with PECVD glass or leaving them uncovered have been tested. Still the results showed very high losses, which were comparable to the loss of the modes propagating in the silica buffer layer.

By increasing the dimensions of the waveguide it becomes multi-moded, and in principle some considerations about mode profiles and mode-coupling should be taken into account. However at this stage of the waveguide analysis, these issues are of no importance and have therefore been ignored.

2.4.1 Possible improvements

In the papers published concerning the issue of decreasing the loss in waveguides fabricated in LPCVD silicon, further processing steps, which include hydrogenation, were carried out after the fabrication of the waveguides [30]. The hydrogenation method showed very good results and was performed using four different techniques, which make use of dedicated equipment not available in this work. Due to these limitations it was not possible to pursue this kind of investigations further.

2.5 Conclusion

The main goal was to develop an alternative method to fabricate SOI-substrates intended for use in integrated optics and therefore with specific optical properties, such as low loss at the telecommunication wavelength at 1300 and 1550 nm. The conventional fabrication methods are expensive and involve many complicated process steps. In this work the fabrication of such a substrate by oxidation of a standard wafer followed by deposition of silane (SiH_4) in a LPCVD process has been investigated. The properties of the silicon formed from the LPCVD process depends on the deposition parameters. An important issue is scattering from both the interface roughness and the bulk of the deposited silicon. The interface roughness has been reduced by lowering the deposition temperature.

By lowering the deposition temperature, the silicon is deposited in its amorphous state, which has a higher loss than the poly-crystalline state. An attempt to reduce the bulk loss of the amorphous state has been performed by annealing the silicon films, whereby the silicon becomes poly-crystalline. The anneal process was carried out at 800°C and 1100°C, respectively. The loss has been evaluated by fabricating strip waveguides in the fabricated silicon films and subsequently measuring their transmission losses using the cut-back method. The interaction of light modes with the waveguide depends on the geometrical structure of the waveguide. This have been elucidated by making waveguides with different thicknesses: 300 nm and 2.0 μm and different cladding materials: air and glass. In spite of all these parameters the experiments revealed that the fabricated waveguides had a very high insertion loss >65–70 dB for waveguides with a length of only 4 mm.

Comparison with theoretical and experimental results in the literature showed that the surface scattering loss could not account for the measured loss value. Therefore the high loss of the fabricated waveguides is attributed to the intrinsic structure of the deposited silicon, which could not be investigated further, due to both limitations in time and available equipment. It was therefore decided to stop the material investigation at this point and focus on fabricating photonic crystals applying commercial SOI. The remaining chapters are devoted to this subject.

Chapter 3

Theory and Numerical Simulation

In this chapter the theory behind the photonic bandgap effect will briefly be sketched. Two theoretical methods have been used extensively in calculating different optical properties of the photonic crystals. The plane wave expansion method has been used to calculate band-diagrams and field distributions in specific photonic crystal structures. The finite-difference time-domain method has been applied to simulate the wave propagation and transmission characteristics of the photonic crystals. It has been shown that there is a good correspondence between the results obtained from these two simulations methods, and most importantly there is also a very good agreement between the simulated results, using a 3D finite-difference time-domain method, and experimental results [51]. The simulated results therefore usually give very good estimations of how a given component actually performs.

3.1 Maxwell's equations

Light is classically described as electromagnetic radiation which propagation properties are governed by the complete set of macroscopic Maxwell's equations. On the differential form these are given by [52]:

$$\nabla \cdot \mathbf{D}(\mathbf{r},t) = \rho(\mathbf{r},t) \tag{3.1}$$

$$\nabla \cdot \mathbf{B}(\mathbf{r},t) = 0 \tag{3.2}$$

$$\nabla \times \mathbf{E}(\mathbf{r},t) = -\frac{\partial \mathbf{B}(\mathbf{r},t)}{\partial t} \tag{3.3}$$

$$\nabla \times \mathbf{H}(\mathbf{r},t) = \mathbf{J}(\mathbf{r},t) + \frac{\partial \mathbf{D}(\mathbf{r},t)}{\partial t} \tag{3.4}$$

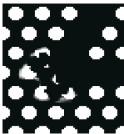

where the usual notation for the four fields is used: *electric displacement field* ($\mathbf{D}$), *magnetic induction field* ($\mathbf{B}$), *electric field* ($\mathbf{E}$), *magnetic field* ($\mathbf{H}$), and where ρ and $\mathbf{J}$ denote the *free charges* and *free currents*, respectively. The electromagnetic fields are related by the constitutive relations:

$$\mathbf{D} = \varepsilon\mathbf{E} = \varepsilon_{\mathrm{r}}\varepsilon_0\mathbf{E} \tag{3.5}$$

$$\mathbf{B} = \mu\mathbf{H} = \mu_{\mathrm{r}}\mu_0\mathbf{H} \tag{3.6}$$

where the material properties are contained in ε and μ which are the dielectric function (or *permittivity*) and the *permeability*, respectively.

3.1.1 Simplifications

For materials usually considered in optics some simplifications to the above mentioned set of equations are applicable. It is assumed that the materials are isotropic, material losses are negligible, and that the materials are operated in the linear regime so that ε and μ are real functions independent of the magnitude and direction of the fields. It is also assumed that ε and μ are independent of frequency, thereby ignoring material dispersion. Using these assumptions, and letting $\rho = 0$ and $\mathbf{J} = 0$, the equations can be rewritten in a form only containing the electric and magnetic fields by inserting the constitutive relations, equation (3.5) and (3.6), into equation (3.3) and (3.4):

$$\nabla \times \mathbf{E}(\mathbf{r}, t) = -\mu\frac{\partial\mathbf{H}(\mathbf{r}, t)}{\partial t} \tag{3.7}$$

$$\nabla \times \mathbf{H}(\mathbf{r}, t) = \varepsilon\frac{\partial\mathbf{E}(\mathbf{r}, t)}{\partial t} \tag{3.8}$$

For non-magnetic materials, as considered here, the permeability is set equal to the vacuum permeability, so that $\mu = \mu_0 \Rightarrow \mathbf{B} = \mu_0\mathbf{H}$, and the material properties are contained entirely in the dielectric constant $\varepsilon = \varepsilon(\mathbf{r})$.

It is solutions to this set of equations that are sought for a given electromagnetic problem, where any structural element is defined through $\varepsilon(\mathbf{r})$. These can very seldom be obtained analytically, and it is therefore necessary to use numerical techniques for obtaining the solutions of a given problem. Two such methods have been used, namely the plane wave expansion method and the finite-difference time-domain method, as described in the following.

3.2 Plane wave expansion

The plane wave expansion method (PWE) consists of expressing the fields as a superposition a harmonic plane waves, which are simple solutions to Maxwell's equations. This allows for the Maxwell's equations to be rewritten into an eigenvalue problem. The essence of the PWE method is that due to the periodicity of the dielectric function it can be expanded into a discrete fourier series.

Eigenvalue equation

It is convenient to work in the frequency domain and thereby expressing the fields with a harmonic time dependence:

$$\mathbf{H}(\mathbf{r},t) = \mathbf{H}(\mathbf{r})e^{i\omega t} \tag{3.9}$$

$$\mathbf{E}(\mathbf{r},t) = \mathbf{E}(\mathbf{r})e^{i\omega t} \tag{3.10}$$

By inserting these expressions into equation (3.7) and (3.8) the following expressions are obtained:

$$\nabla \times \mathbf{E}(\mathbf{r}) = -i\omega\mu_0\mathbf{H}(\mathbf{r}) \tag{3.11}$$

$$\nabla \times \mathbf{H}(\mathbf{r}) = i\omega\varepsilon(\mathbf{r})\mathbf{E}(\mathbf{r}) \tag{3.12}$$

from which the electric field can be eliminated leading to an equation involving only the magnetic field:

$$\nabla \times \left\{ \frac{1}{\varepsilon_{\mathrm{r}}(\mathbf{r})} \nabla \times \mathbf{H}(\mathbf{r}) \right\} = \frac{\omega^2}{c^2}\mathbf{H}(\mathbf{r}) \tag{3.13}$$

where $\varepsilon_{\mathrm{r}}(\mathbf{r}) = \varepsilon(\mathbf{r})/\varepsilon_0$ is the relative dielectric constant and $c = 1/\sqrt{\varepsilon_0\mu_0}$ is the velocity of light in vacuum. Equation (3.13) is a Hermitian eigenvalue problem, where $\mathbf{H}$ represents the *eigenvector* and $\frac{\omega^2}{c^2}$ is the corresponding *eigenvalue* [53].

3.2.1 Dispersion relation

Many of the optical properties of photonic crystals can be revealed by the *dispersion relation* or *band-diagram* of the given structure. The *dispersion relation* can be calculated by solving equation (3.13) and plotting the frequency ω as a function of the wave-vector $\mathbf{k}$.

Homogeneous media

For a homogeneous media, where ε_{r} is constant, simple solutions to equation (3.13) are plane-waves:

$$\mathbf{H}(\mathbf{r},t) = \mathbf{H}_0 e^{i(\mathbf{k}\cdot\mathbf{r}-\omega t)} \tag{3.14}$$

where $\mathbf{k}$ is the wave-vector indicating the propagation direction of the wave and ω is the angular frequency. In a homogenous medium mono-chromatic plane waves propagate with a speed given by:

$$v = \frac{c}{\sqrt{\varepsilon_{\mathrm{r}}}} = \frac{c}{n} = \frac{\omega}{||\mathbf{k}||} = \frac{\omega}{k} \tag{3.15}$$

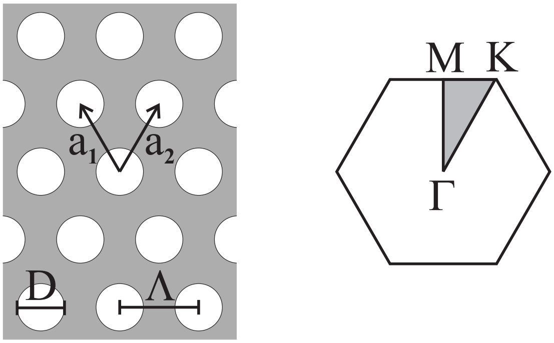

Figure 3.1: The real space hexagonal lattice (left) and the reciprocal lattice (right) of a photonic crystal defined by holes in a dielectric material. The irreducible brillouin-zone is depicted by the grey triangle.

where n is the refractive index of the medium. The *dispersion relation* is found by plotting ω as a function of k:

$$\omega(k) = \frac{ck}{n} \tag{3.16}$$

which is just a straight line with slope $\frac{c}{n}$. When considering two-dimensional photonic crystal slabs this line is referred to as the air-line for an air cladding or the silica-line for a silica cladding.

Periodic structures

The picture changes dramatically when looking at a material with a discrete translational symmetry so that:

$$\varepsilon_{\mathrm{r}}(\mathbf{r}) = \varepsilon_{\mathrm{r}}(\mathbf{r} + \mathbf{R}) \tag{3.17}$$

where $\mathbf{R}$ is a lattice vector that translates the lattice into itself. The set of lattice vectors can in two dimensions be written as:

$$\mathbf{R} = n\mathbf{a}_1 + m\mathbf{a}_2 \tag{3.18}$$

where $\mathbf{a}_i, i = 1, 2$ are the primitive lattice vectors shown in the left part of figure 3.1 for a hexagonal lattice of holes, and n, m are integer numbers. For periodic structures it is a more complicated task to solve equation (3.13). However, because of the discrete translational symmetry of the material, the dielectric function $\varepsilon(\mathbf{r})$ can be written as a discrete fourier series in the reciprocal lattice vectors $\mathbf{G} = n'\mathbf{b}_1 + m'\mathbf{b}_2$ where $\mathbf{b}_j, j = 1, 2$ is defined by the primitive lattice vectors according to $\mathbf{a}_i \cdot \mathbf{b}_j = 2\pi\delta_{ij}$ and n', m' are integer numbers [53]. Thus the dielectric function can be written as:

$$\frac{1}{\varepsilon(\mathbf{r})} = \sum_{\mathbf{G}} \varepsilon^{-1}(\mathbf{G}) e^{i\mathbf{G}\cdot\mathbf{r}} \tag{3.19}$$

The periodicity of the structure also implies that Bloch's theorem can be applied to the modal solutions of the magnetic field, which then can be written as:

$$\mathbf{H}(\mathbf{r}) = \mathbf{H}_{\mathbf{k}n}(\mathbf{r}) = \mathbf{u}_{\mathbf{k}n}(\mathbf{r}) e^{i\mathbf{k}\cdot\mathbf{r}} \tag{3.20}$$

where $\mathbf{u}_{\mathbf{k}n}(\mathbf{r}) = \mathbf{u}_{\mathbf{k}n}(\mathbf{r}+\mathbf{R})$. The different solutions are indexed by n with increasing ω. Because $\mathbf{u}_{\mathbf{k}n}(\mathbf{r})$ has the same periodicity as the dielectric function it can also be written as a discrete fourier series in the reciprocal lattice vectors $\mathbf{G}$. By insertion into equation (3.20) this leads to the following expression for solutions of the magnetic field:

$$\mathbf{H}_{\mathbf{k}n}(\mathbf{r}) = \sum_{\mathbf{G}} \sum_{\lambda=1}^{2} h_{\mathbf{k}n,\lambda}(\mathbf{G}) \hat{\mathbf{e}}_\lambda e^{i(\mathbf{k}+\mathbf{G})\cdot\mathbf{r}} \tag{3.21}$$

where $h_{\mathbf{k}n}$ are the expansion coefficients of $\mathbf{u}_{\mathbf{k}n}(\mathbf{r})$ and $\hat{\mathbf{e}}_\lambda, \lambda = 1, 2$ are unit vectors assuring the transversality condition $\nabla \cdot \mathbf{H} = 0$ by letting $\hat{\mathbf{e}}_\lambda \cdot (\mathbf{k}+\mathbf{G}) = 0$. Inserting equation (3.19) and (3.21) into equation (3.13) the following matrix equation is obtained:

$$\sum_{\mathbf{G}'} |\mathbf{k}+\mathbf{G}||\mathbf{k}+\mathbf{G}'| \varepsilon(\mathbf{G}-\mathbf{G}') \begin{bmatrix} \hat{\mathbf{e}}_\mathbf{2} \cdot \hat{\mathbf{e}}'_\mathbf{2} & -\hat{\mathbf{e}}_\mathbf{2} \cdot \hat{\mathbf{e}}'_\mathbf{1} \\ -\hat{\mathbf{e}}_\mathbf{1} \cdot \hat{\mathbf{e}}'_\mathbf{2} & \hat{\mathbf{e}}_\mathbf{1} \cdot \hat{\mathbf{e}}'_\mathbf{1} \end{bmatrix} h_{\mathbf{G}',\lambda'} = \frac{\omega^2}{c^2} h_{\mathbf{G},\lambda} \tag{3.22}$$

A fully detailed derivation of the matrix equation can be found in [54]. In this work the eigenvalue problem is solved by a method where the fully-vectorial eigenmodes of Maxwell's equations with periodic boundary conditions are computed by preconditioned conjugate-gradient minimization of the block Rayleigh quotient in a plane wave basis, using a freely available software package [55]. Details on the underlying calculation method can be found in [56, 57].

The structure is defined by the dielectric function within a unit cell repeated throughout space, as depicted in figure 3.2 A) for circular holes in silicon, where the unit cell is encircled by the red dashed line. Having defined the structure the solutions for a given $\mathbf{k}$, characterized by the frequency $\omega_n(\mathbf{k})$ and the corresponding field distributions (modes) $\mathbf{H}_{\mathbf{k}n}(\mathbf{r})$, can be obtained from solving equation (3.13). Due to the form of the modal-field solutions from Bloch's theorem in equation (3.20) we have $\mathbf{H}_{\mathbf{k}n} = \mathbf{H}_{(\mathbf{k}+\mathbf{G})n}$, and all possible solutions for the complete structure can be obtained entirely from k-vectors in the first brillouin-zone [53, 58]. As a result of the rotational symmetry of the structure it is only

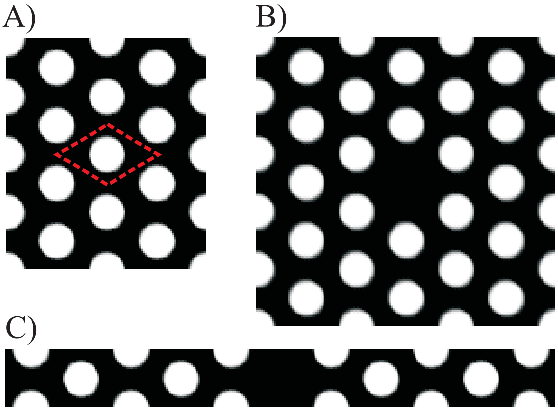

Figure 3.2: Examples of cells used in plane wave expansion calculations. The complete structure is obtained by repeating the cell throughout space. A) a single cell, encircled by the red dashed line, used to simulate a complete photonic crystal without defects. B) a single hole defect (cavity) and C) a single line defect (waveguide). The waveguide line defect is in the (Γ–K)-direction of the photonic crystal lattice.

necessary to find solutions at k-points along the boundary of the irreducible brillouin-zone illustrated by the grey triangle defined by the three symmetry points: Γ, M, K in the right part of figure 3.1. By plotting the calculated ω as a function of $\mathbf{k}$ along the lines between these symmetry points a band-diagram is obtained.

3.2.2 Modes and Polarization

The allowed modes and their frequencies in a given structure are characterized by the field solutions $\mathbf{H}_{\mathbf{k}n}(\mathbf{r})$ and ω. For 2D structures the allowed modes can be classified into two distinct polarizations [53]:

1. Transverse Electric (TE) polarization, where the electric field is confined to the xy-plane $\mathbf{E} = (E_x, E_y, 0)$ and $\mathbf{H} = (0, 0, H_z)$

2. Transverse Magnetic (TM) polarization, where the Magnetic field is confined to the xy-plane $\mathbf{H} = (H_x, H_y, 0)$ and $\mathbf{E} = (0, 0, E_z)$

For a photonic crystal defined in a slab-structure, the modes are not purely TE or TM modes but designated as being TE-like or TM-like. These modes are classified by how they transform under the horizontal mirror operation in the middle of the slab. TE-modes are even under reflection and TM-modes are odd [59]. However, these modes have strong similarities with the TE-modes and TM-modes in two dimensions [6], and are here therefore just referred to simply as TE- and TM-modes or TE- and TM-polarization.

Figure 3.3 shows a band-diagram of a photonic crystal for both TE- and TM-polarizations, calculated in 2D using the above mentioned software package. The structure consists of circular holes with $\varepsilon = 1$ in a material with $\varepsilon = 12$, corresponding to air holes in silicon. The holes are ordered in a hexagonal lattice, as depicted in the left side of figure 3.1, with a ratio between the hole diameter and lattice period $D/\Lambda = 0.75$. Due to the scalability of Maxwell's equations it is very common to use normalized frequencies $\omega = \Lambda/\lambda$ where Λ is a characteristic length equal to the lattice period and λ is the wavelength corresponding to ω. In figure 3.3 it is seen that there is no solution for frequencies between 0.23–0.36 for the TE-polarization and hence a bandgap is obtained. For the TM-polarization there is no band gap. However the bandgap will open for the TM-polarization if the hole radius is increased to $\sim 0.4\Lambda$ [60, 61].

3.2.3 Waveguides and Cavities

As mentioned above a structure is defined by repeating a single cell throughout space. The cell is simple when considering a photonic crystal without defects, see figure 3.2 A). In the case where the structure contains a cavity and/or a waveguide it is necessary to define a super-cell. Figure 3.2 B) and C) show super-cells for a cavity and a waveguide, respectively. When considering such components it is important to have a significant spacing between the defects in adjacent cells, in order to avoid coupling between the defect states, as this could lead to band-broadening. Usually 4–5 lattice periods are sufficient [61]. In case of a single line defect the crystal symmetry is broken and the discrete translational symmetry only persists along the line defect. The corresponding k-vectors are then projected onto this direction [62], and only this direction is used when plotting the band-diagram of a single line defect. This situation is shown in the left part of figure 3.4. By comparison to the band-diagram in figure 3.3 it can be seen that by introducing the line-defect modal solutions, shown with the red and blue lines, are allowed in the band-gap of the original crystal lattice.

3.3 Finite-difference time-domain method

The propagation of light in the photonic crystal can be numerically simulated by using the finite-difference time-domain (FDTD) method. The FDTD method basically consists of approximating the space and time derivatives by finite differences in Maxwell's equations, that this way can be solved numerically by time-stepping the propagation of the fields. This method has found widespread

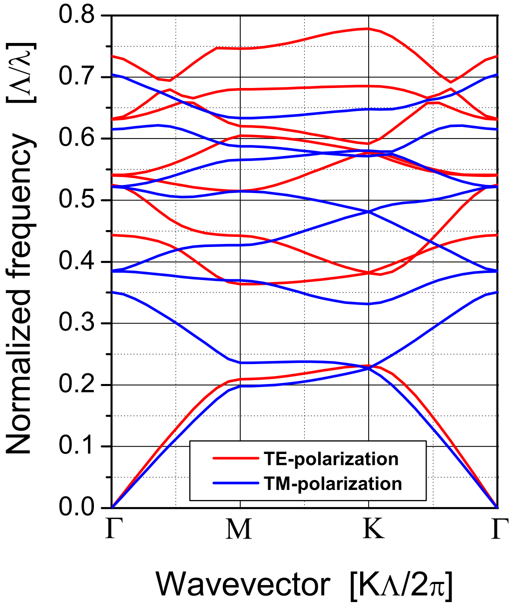

Figure 3.3: A band diagram of a hexagonal lattice with $D/\Lambda = 0.75$ of low-index material in a high-index material having $\varepsilon = 1$ and $\varepsilon = 12$ respectively. The band diagram was calculated using the the software package from MIT.

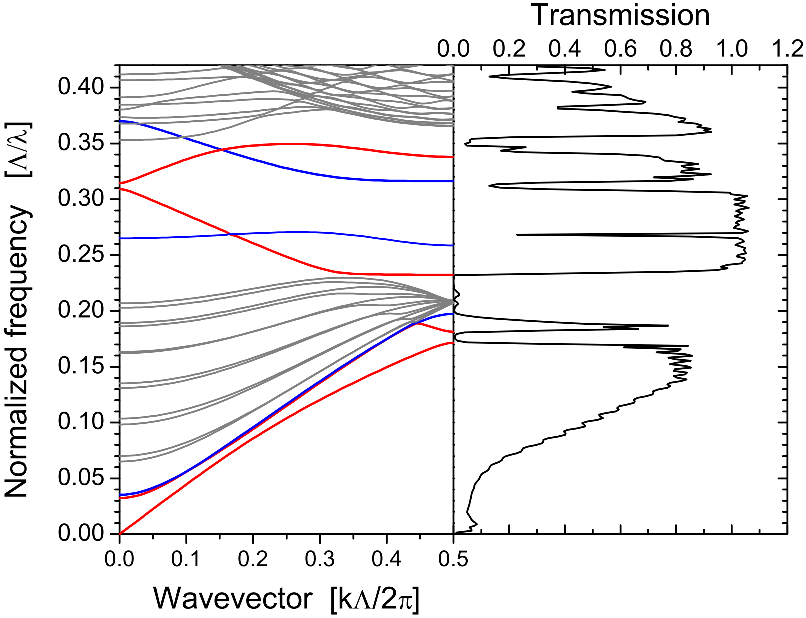

Figure 3.4: The left part shows the band-diagram of a single line defect photonic crystal waveguide. The modes are TE-polarized and are divided into laterally even (red line) and odd (blue line). Index guided modes are seen below the band gap. The grey lines correspond to slab modes. The calculation is performed using the plane wave expansion method, with the super-cell shown in figure 3.2 C). The right part shows the transmission calculated using the finite-difference time-domain method. Both calculations are performed in 2D.

use in modelling the wave-propagation in photonic crystals as it is very flexible concerning structure geometries and can handle large index variations [63]. In this section there will be a short description on the simulation method and its relation to the band-diagrams from last section. The calculations were performed using a commercial software package *Crystalwave* from *Photon Design*[1]. The software is based on the program code described in [51].

3.3.1 Discretization

In the FDTD method the structure under investigation is divided into a finite lattice of grid points, on which the field values are calculated. Several schemes for performing FDTD simulations can be applied [63]. Here the FDTD scheme is implemented on coinciding space grids for the magnetic and electric fields. The space and time derivatives are expressed using *Forward Differences* for the electric field and *Backward Differences* for the magnetic field [64]. Using this scheme the derivatives in Maxwell's equations (3.7) and (3.8) for the electric and magnetic field are replaced by the following expressions [65]:

$$\frac{\partial E(\mathbf{r},t)}{\partial r_i} \rightarrow \frac{\Delta_i^+ \hat{E}}{\Delta r_i} = \frac{\hat{E}(\mathbf{r}+q_i\mathbf{u}_i,t)-\hat{E}(\mathbf{r},t)}{q_i} \tag{3.23}$$

$$\frac{\partial E(\mathbf{r},t)}{\partial t} \rightarrow \frac{\Delta_i^+ \hat{E}}{\Delta t} = \frac{\hat{E}(\mathbf{r},t+\delta t)-\hat{E}(\mathbf{r},t)}{\delta t} \tag{3.24}$$

$$\frac{\partial H(\mathbf{r},t)}{\partial r_i} \rightarrow \frac{\Delta_i^- \hat{H}}{\Delta r_i} = \frac{\hat{H}(\mathbf{r},t)-\hat{E}(\mathbf{r}-q_i\mathbf{u}_i,t)}{q_i} \tag{3.25}$$

$$\frac{\partial H(\mathbf{r},t)}{\partial t} \rightarrow \frac{\Delta_i^- \hat{H}}{\Delta t} = \frac{\hat{H}(\mathbf{r},t)-\hat{H}(\mathbf{r},t-\delta t)}{\delta t} \tag{3.26}$$

where the geometrical space is spanned by the unit-vectors $\mathbf{u}_i$ that define the calculation lattice and q_i is the distance between grid-points in the lattice. The rescaled fields are given by:

$$\hat{E} = q_i E \qquad \text{and} \qquad \hat{H} = q_i H \tag{3.27}$$

The idea can be generalized into an arbitrary coordinate system [65], but in the implementation used here only the cartesian space is considered. The introduction of the rescaled fields can however be useful when considering a calculation grid with an unequal spacing in the three spatial directions. The coordinate system used in the FDTD simulations is defined in such a way that the x-direction and z-direction are along the (Γ–M)-direction and (Γ–K)-direction of the crystal, respectively. The y-direction is in the vertical direction, perpendicular to the crystal plane. In order to comply with the hexagonal geometry of the structures considered here, the coordinate-grid is rectangular with a grid-spacing

---

[1] *http://www.photond.com*

$q_x = \sqrt{3} \cdot q_z$. By defining the grid-spacing as the period of the crystal lattice divided by an even integer, the rectangular geometry will ensure that there is an integer number of grid-points between the crystal lattice points in both the x and z–direction. This way spectral features arising from the periodicity of the structures could be well represented in the numerical simulations [66]. The grid-spacing in the y-direction is automatically set equal to the grid-spacing in the z-direction: $q_y = q_z$.

Time stepping

By applying the above mentioned finite differences scheme all the field components of the two fields can at a given time step be expressed by the field values of the previous time step [67]. The FDTD algorithm calculates the electric and magnetic fields at fixed time intervals defined by the time-step δt. The evolvement of the fields are then performed by a discrete time-stepping on the discrete spatial grid. In order to have an efficient and reliable FDTD calculation some considerations have to be made about the size of the time step. If the time-step is too short then the calculation will take an unnecessary amount of time. If the time-step is too long the calculation will be unstable. The stability is automatically ensured by the FDTD program by setting the time interval small enough to fulfill the *Courant stability criterion*, which for the rectangular lattice described above is given by [66]:

$$\delta t = 0.99\sqrt{\frac{3}{7}}\left(\frac{q_x}{c}\right) \tag{3.28}$$

where q_x is the grid spacing in the x–direction. The space grid and time step are linked through the above expression, which means that for finer spatial grid, a larger number of time steps is needed in order to simulate the same total amount of time.

3.3.2 Excitors and Sensors

In order to model the propagation of light through a certain structure, an initial wave field has to be defined. This is done by a wave excitor, which is a time varying field applied with a certain initial spatial field distribution, usually placed at the input position of the structure. Different types of excitors are available, and the choice depends on the kind of properties of the photonic crystal that need to be investigated.

To extract information about the transmission characteristics of a given structure, sensors have to be positioned both at the input and output positions of the crystal. A sensor defines a line (in 2D) or a plane (in 3D) of grid points where the field or the flux is recorded at all time steps during the simulation.

By placing a sensor at the input position a normalized transmission through a specific output sensor can be obtained. Several sensors can be defined in the structure simultaneously.

A plane wave excitor generates a broad-band initial pulse and can be used to calculate the spectral transmission characteristics of a given structure. The spectral information of the flux is extracted by performing a fast fourier transform (FFT) of the temporal values recorded by the sensors.

The right part of figure 3.4 shows the result for a FDTD transmission calculation of a photonic crystal with a single line defect performed using a plane wave excitor. The transmission is shown on the horizontal axis as a function of the normalized frequency on the vertical axis. The photonic crystal structure is identical to the one used in the band-diagram calculation shown in the left part of figure 3.4 and the transmission properties can be directly related to the band-diagram. The high transmission region from $\omega = 0.23$ to $\omega = 0.31$ correlates very well with the even bandgap mode. The mini-stop band at $\omega = 0.27$ is a numerical artifact since the transmission dip reduces by increasing the spatial resolution. It is caused by a forced artificial anti-crossing in the FDTD calculation of the even and odd mode at that frequency [51]. High transmission is also observed for the index-guided mode below $\omega = 0.17$. In general the calculated dispersion relation nicely explains the transmission properties of the photonic crystal waveguide, as described in more detail in [51].

It is also possible to use single frequency excitors with different types of time envelopes. These can be used to gain information of how the fields evolve and distribute throughout the structure as time progresses by plotting the field at all grid points at a certain time step. In figure 3.5 two field plots is shown for A) $\omega = 0.21$ and B) $\omega = 0.28$, which is outside and inside the bandgap, respectively. In the plots a steady state situation is reached that occurs after a sufficiently high number of time steps. When the frequency is located outside the band gap the field is clearly poorly confined to the line defect, since the electromagnetic modes are now allowed to propagate in the surrounding crystal structure and are diffracted to spread out across the whole structure. The opposite is true when the normalized frequency is inside the bandgap and the modes are not allowed to propagate in the surrounding crystal structure and thereby they can only exist along the line defect.

3.3.3 Perfectly matched layers

In the band-diagram calculations by the PWE method the symmetry of the structure can be exploited and it is sufficient only to include the basic cell in a calculation. This is contrary to the FDTD method where the complete structure has to be modelled, and special attention has to be made about the termination of the calculation region. A very widely used method is to apply perfectly

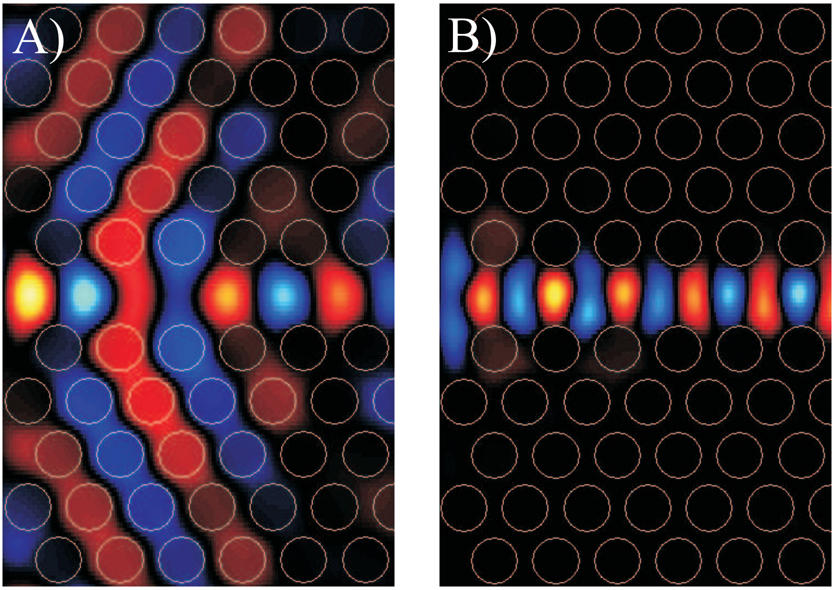

Figure 3.5: The field distribution in a single line defect photonic crystal after a sufficiently long period of time has elapsed to ensure that the steady state has occurred. The structure has $D/\Lambda = 0.75$. The normalized frequency is A) $\omega = 0.21$ and B) $\omega = 0.28$, which is outside and inside the bandgap, respectively.

matched layers (PML) around the structure. In these layers an incident light field will be absorbed and thereby unwanted reflections back into the structure are avoided. Several types of PML has been suggested. Details of the PML used in this programme can be found in [51].

The two modelling methods described in this section have been used as tools for gaining information about the properties of specific structures. Usually these methods do not provide any information about how to achieve a desired functionality or how to improve the performance of a given component under investigation. The next chapter deals with different methods used to address this point.

Chapter 4

Design

In the previous chapter methods for calculating the transmission and band diagrams were sketched out. These calculations do not provide any information on how to achieve a desired performance. The optimization of the performance of a given type of component is normally done by changing the design parameters mostly by trial-and-error, guided by intuition and experience. So far such approaches have mainly been limited to adding or removing holes, changing the diameter and/or changing the position of selected holes in the photonic crystal structures. This approach has been used extensively for designing several simple components such as bends [68,69], splitters [70–72] and couplers [8,73]. Recently, however some tools for achieving good designs have been made available. In the first part of this chapter an inverse design method called *topology optimization* adopted from mechanical engineering will be described. This method has been used in this work to design several components with a high transmission in a broad wavelength range. Narrow band filter functionalities need some special consideration, and in this connection a method based on momentum space design has been used to investigate a wavelength selective element, which is essential in an add-drop multiplexer.

4.1 Topology optimization

Recently there has been an increasing interest using inverse design techniques to designing photonic crystal structures [74]. There are several approaches to solve such inverse design problems. Optimization of the properties of band gap structures has been performed by using methods such as *level-sets* [75], *evolution algorithm* [76], *gradient descent* [77], and *topology optimization* [78]. In the work presented below the *topology optimization* method has been used. The method is adopted from mechanical engineering and has found widespread use in a number

of different branches of research activities [79,80]. Most recently the method has been used to optimize the performance of photonic crystal components such as a bend and a splitter in a quadratic lattice of dielectric rods in air [81,82].

In this work a photonic crystal z-bend made in a hexagonal lattice of holes in a dielectric material has been investigated. This is a difficult and challenging design problem in order to achieve good transmission and large bandwidth, and it could serve as an excellent benchmark for the method. A brief introduction to topology optimization method is given in the following.

4.1.1 System equation

As a starting point a photonic crystal having holes with a dielectric constant $\varepsilon_r = 1$ arranged in a hexagonal lattice in a material with $\varepsilon_r = 12$ is considered. This structure corresponds to air-holes in silicon and is known to possess a bandgap for TE-polarized light, see section 3.2.1. The wave propagation is modelled using a 2D frequency-domain method. For the TE-polarization and assuming harmonic waves $u(\mathbf{x}, t) = u(\mathbf{x})e^{-i\omega t}$, where ω is the wave frequency, the governing equation in a domain Ω is given by:

$$\nabla \cdot \left(\frac{1}{\varepsilon_r} \nabla u \right) + \frac{\omega^2}{c^2} u(\mathbf{x}) = 0 \quad \text{in} \quad \Omega \tag{4.1}$$

where $\varepsilon_r(\mathbf{x})$ denotes the dielectric constant of the involved materials, $u(\mathbf{x})$ is the field in the plane containing the structure $\mathbf{x} = (x, y)$. For the TE-polarization, the field $u(\mathbf{x})$ corresponds to the z-component of the magnetic field H_z.

Discretization

The implementation is based on the finite element method (FEM) [83]. By applying the finite element procedure the following discretized system-equation can be obtained [80,82]:

$$\mathbf{S}(\omega)\mathbf{u} = \mathbf{f}(\omega) \tag{4.2}$$

with $\mathbf{S}(\omega) = (\mathbf{K} + i\omega\mathbf{C} - \omega^2\mathbf{M})$. In this expression $\mathbf{f}(\omega)$ is a force term that models a harmonic incident wave and $\mathbf{C}$ is a damping matrix that model absorbing boundary conditions and/or structural damping [80]. For optical systems the structural damping is included as an additional conductance term. The above equation is solved for $\mathbf{u}$ which contains the discretized values of the field.

The initial material distribution is build from a regular hexagonal lattice, where the photonic crystal z-bend waveguide is simply formed by removing holes along the (Γ–K)-direction of the crystal, as shown in figure 4.1. The structure is defined in a domain Ω, which is discretized using square elements. Due the periodicity of the initial structure, the structure can be build up from simple blocks, as shown enlarged in the figure. Each block consists of 7×12 square

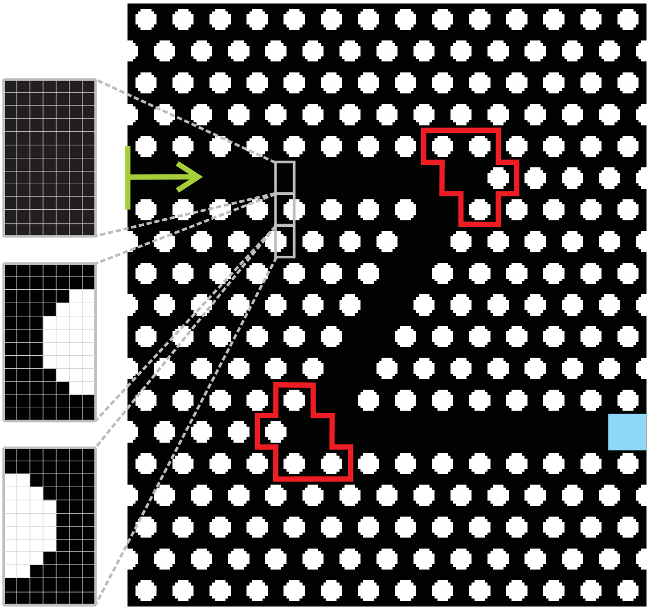

Figure 4.1: An image of a z-bend component showing the initial material distribution used as the starting point in the topology optimization. The enlargements to the left show the discretization of the basic building blocks each consisting of 7×12 square elements used in the FEM analysis. The green arrow illustrates the incident wave. The design domain (Ω_D) is encircled by the red line. The Poynting-vector is maximized in the blue area (Ω_P) at the output port.

elements. This assures that the geometry resembles that of a hexagonal lattice when the blocks are put together to form the complete structure. The complete computational domain also includes perfectly matched layers at the input and output port to eliminate unwanted reflections [82]. The computational domain is constituted of $[(28 \times 19) + 2 \times (22 \times 11)] \times 7 \times 12 = 85344$ elements in total. Solving for a single frequency takes about 5 seconds on a 2.66 GHz computer with 1 Gb RAM.

4.1.2 Objective Function

The goal is to optimize the transmitted optical power through an optical component. The energy flow for electro-magnetic wave propagation is given by the

time averaged Poynting-vector [82]:

$$\mathbf{P}(\mathbf{x}) = \frac{\omega}{2} A \Re(i u^* \nabla u) \tag{4.3}$$

where u^* is the complex conjugate of the field.

The design goal is to maximize the transmitted power through the component. A suitable objective function for the optimization is the component of the Poynting-vector in the output direction P^{out} averaged over all finite elements in a domain Ω_{P} located at the output position:

$$P^{\text{out}} = \frac{1}{N} \sum_{e \in \Omega_{\text{P}}} P_e^{\text{out}} \tag{4.4}$$

as depicted as the blue area in figure 4.1. The area shown encircled by the red lines in the figure is the design domain Ω_{D}. The incident wave is depicted with a green arrow. By changing the material distribution in Ω_{D} the objective function will change accordingly. The optimization problem can be formulated as:

$$\max_{x_e} P^{\text{out}}(\omega) \tag{4.5}$$

which is achieved by iteratively changing the material composition in the design domain. A direct way to find a optimum solution could be to try out all possible combination of distributing the material in the design domain. Consider a design domain consisting of N elements. If an optimum is assumed to exist when half of the elements is material 1 and the other half is material 2, then the number of combinations is given by $N!/(N-M)!M!$, where $M = N/2$, which is a very large number even for rather small values of N. Therefore this direct way is a very impractical method. However methods exist that dictate how to iteratively redistribute the material in more clever ways.

4.1.3 Sensitivity Analysis

In topology optimization a continuous approach is applied where each element within Ω_{D} is assigned to one design variable ρ_e:

$$0 \leq \rho_e \leq 1, \;\; e \in \Omega_{\text{D}} \tag{4.6}$$

and thereby the elements are allowed to have intermediate values between material 1 with ε_{r1} and material 2 with ε_{r2} as expressed by the material interpolation scheme:

$$\varepsilon_{re}^{-1} = \varepsilon_{r1}^{-1} + \rho_e(\varepsilon_{r2}^{-1} - \varepsilon_{r1}^{-1}) \tag{4.7}$$

where ε_{re} is the dielectric constant of the element e. For $\rho_e = 0$ the element will be material 1 and for $\rho_e = 1$ it will be material 2. The objective function is now expressed only as a function of the design variables ρ_e, and the objective function for a given material distribution is computed by solving equation (4.2) and performing the summation over elements in Ω_{P} as described by equation (4.4). The essential part of the sensitivity analysis is then to determine how the objective function changes when the design variables are changed, that is finding the derivatives of the objective function with respect to the design variables. This can effectively be done by the adjoint method [80]:

$$\frac{\partial P^{\mathrm{out}}}{\partial \rho_e} = 2\Re\left(\boldsymbol{\lambda}^T \frac{\partial \mathbf{S}}{\partial \rho_e}\mathbf{u}\right) \tag{4.8}$$

where λ is the solution to the adjoint equation:

$$\mathbf{S}^T\boldsymbol{\lambda} = -\frac{\partial P^{\mathrm{out}}}{\partial \mathbf{u}}\mathbf{u}^* \tag{4.9}$$

Solving this equation only requires to solve equation (4.2) with an extra load term, which can be computed very easily using a factorization method [81, 82].

The actual optimization procedure is based on the method of moving asymptotes (MMA) [84]. The essence of the MMA algorithm is to suggest a transformation of the design variables ρ_e into a new improved material distribution. The design variables ρ_e are updated in accordance with this suggestion, and the objective function is computed again. This procedure is repeated until the design variables have no significant change between successive iterations. The steps in the optimization procedure is summarized in the flow diagram shown in figure 4.2.

Damping and filtering

When performing the topology optimization some problems may arise. Non-unique solutions exist to a given optimized problem and result in multiple local extrema. These can however be smoothed out by a *continuation* method where an artificial damping term is added [78].

It is also possible that the optimized structure will contain elements with intermediate values of the design values $0 < \rho_e < 1$, a structure that is not feasible in the present fabrication processes. Therefore some *penalization* method can be applied which make intermediate values less favorable in the optimization process [82]. Both the *continuation* and the *penalization* are applied through $\mathbf{C}$ in equation (4.2).

In structural mechanics it is necessary to take special care of mesh dependencies. The use of a finer mesh in the finite element analysis will result in the appearance of finer details in the optimized structure. This will eventually pose practical limitations due to fabrication possibilities. When dealing with wave propagation this problem turns out to be of insignificant importance, since the

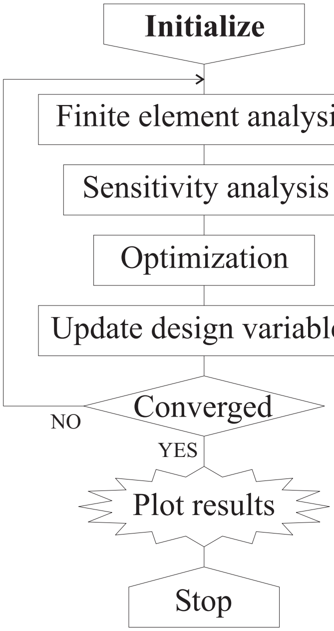

Figure 4.2: A flow diagram showing the different steps that are performed during the optimization procedure. Taken from ref [80].

scattering of waves hardly depends on structural details that are smaller than the wavelength. However, a filter may beneficially be applied in order to avoid unnecessary details [78, 82].

In general, experience has shown that the MMA method is very useful for topology optimization [80]. Since the sensitivities can be calculated with very little computational effort this makes MMA a very efficient method for achieving optimized designs. To this adds the fact that the MMA solver is very flexible as it can be applied to various geometries and behavioral constraints as long as any numerically quantifiable objective function can be defined.

Bandwidth

The topology optimization procedure is performed in the frequency domain for a single frequency at a time. The design goal in this thesis is to have a high transmission (low loss) for a large bandwidth. It turned out that the large bandwidth was automatically obtained from a single frequency for the z-bend described above. For other applications this is not always the case and it is therefore necessary to include more frequencies in the optimization procedure. This is done simply by optimizing the sum of the transmission for a number of frequencies [81], or by applying an active set strategy [82].

The result of performing the topology optimization procedure to the z-bend component, with the initial configuration shown in figure 4.1, is displayed in figure 4.3. No symmetry constrains have been applied in the optimization procedure. The upper left part shows the initial material distribution. The upper right part shows the final material distribution obtained after 900 iterations. In the lower part are shown 5 snapshots, from left to right, of the optimization after 0, 90, 280, 500, 900 iterations. The whole optimization procedure took approximately 2 hours. The transmission through the z-bend is shown in figure 4.4 for the simple (un-optimized) and optimized structure. The transmission curves are normalized to the transmission through a straight waveguide having the same length. It is seen that there is a great improvement in the transmission characteristics both concerning the transmission level and the bandwidth.

FDTD simulation

The topology optimization procedure is only performed in 2D. To get more reliable information about how the optimized structure will perform it is necessary to make a fully 3D FDTD simulation, see section 3.3. The result is shown in figure 4.5, where the performance is now expressed as the loss per bend. In the 3D FDTD simulation the calculation domain consist of a $\Lambda = 420$ nm thick layer of silica below and air above the silicon core. This has been approved to be efficient cladding thicknesses to avoid coupling to the surrounding PML layers. It is observed that the optimized structure shows a much better performance

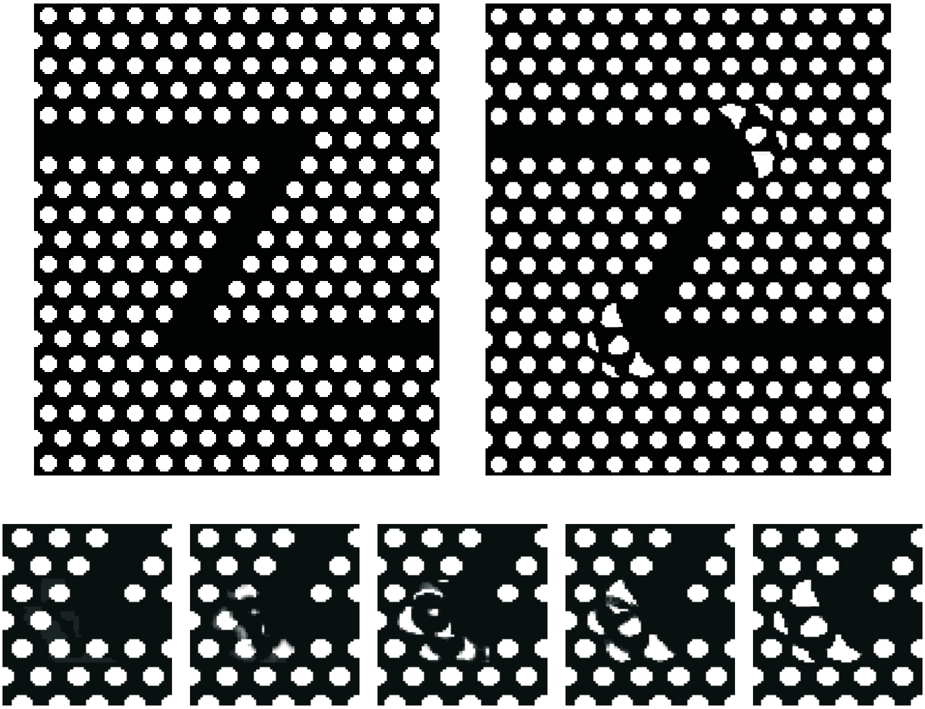

Initial design

90 iterations

280 iterations

500 iterations

Final design

Figure 4.3: The result of applying the topology optimization procedure to the photonic crystal z-bend. The upper left part shows the initial material distribution. The upper right part shows the final material distribution obtained after 900 iterations. The lower part shows 5 snapshots, from left to right, during the optimization procedure after 0, 90, 280, 500, 900 iterations. The optimization procedure took approximately 2 hours.

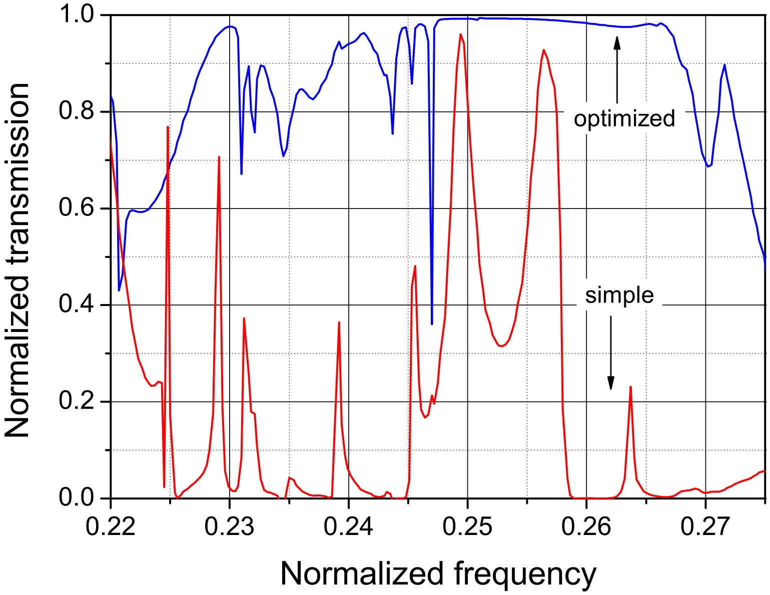

Figure 4.4: The transmission through a photonic crystal z-bend waveguide shown in figure 4.3 for the simple and optimized structure. The transmission curves are normalized to the transmission through a straight photonic crystal waveguide having the same length.

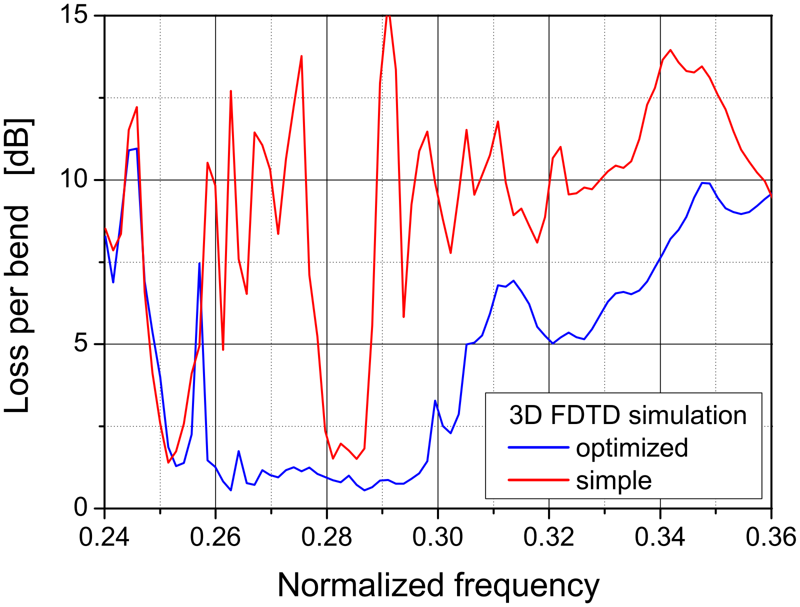

Figure 4.5: 3D FDTD simulations of the bend loss per bend through a z-bend photonic crystal waveguide for TE-polarized light. The red and blue curves are for the simple and optimized structure, respectively. The simulation were performed with a grid-size of $\Lambda/30$ and $2^{15} = 32768$ timesteps.

than the simple structure. The optimized structure shows a very low bend loss in a large bandwidth. The corresponding 2D FDTD simulated field distribution for a normalized frequency $\omega = 0.27$ is shown in figure 4.6. As expected a significantly better guidance through the bend is observed in the case of the topology optimized bend geometry. The topology optimization method has, from a theoretical point of view, proved to be a very efficient modeling tool in achieving good performance of certain selected photonic crystal waveguide components. The optimized structures also show good performance in 3D FDTD simulations. The performance was characterized by a high transmission with a large bandwidth. This is crucial in order to make such components useful in larger systems where utilization of a large bandwidth is important.

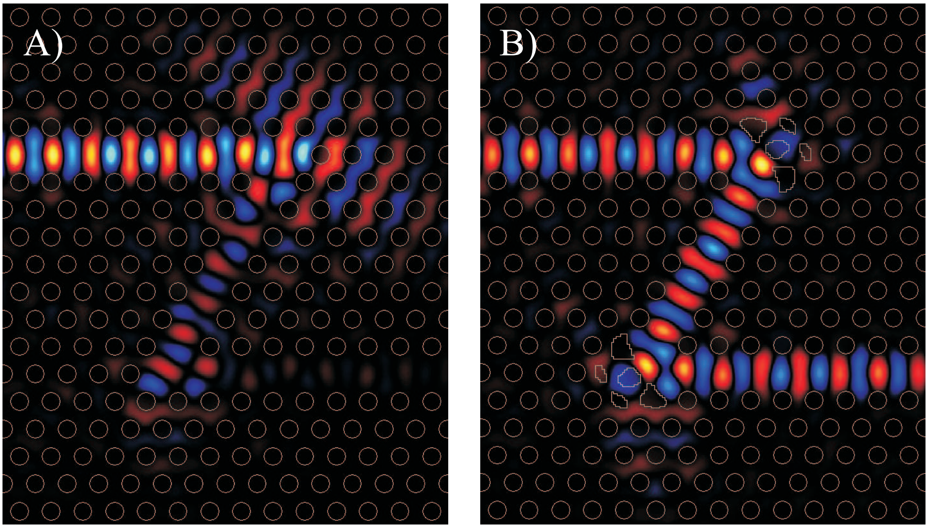

Figure 4.6: A 2D FDTD simulation of the field distribution in z-bend photonic crystal waveguide for TE-polarized light. A) simple z-bend, B) topology optimized z-bend.

Other kinds of functionality, as add-drop filters have a great interest in telecommunication systems. An add-drop filter is characterized with a very narrow wavelength selectivity and has also been tested using the topology optimization, as briefly described in the following.

4.2 Wavelength Selectivity

The functionality of an add-drop filter includes a wavelength selective element. This can be achieved by a cavity resonator, which is made by introducing a single defect into a 2D photonic crystal slab. Different designs of cavities have been proposed. They are categorized as either 1) acceptor defects, where material is moved or 2) donor defects, where material is added, as they resembles the properties of the electronic acceptor/donor states in semi-conductors [85].

Light having a frequency that match the cavity resonance frequency will build up power in the cavity. This way the cavity can function as a wavelength selective element, as it only allows light in a narrow frequency range around the resonance frequency to be built up. The ability to build up power is described by the Q-value of the cavity, and it should be as high as possible for a narrow wavelength selection range.

4.2.1 Q-value

The Q-value is used as a measure of a resonator's ability to build up power. The Q-value of a cavity is given by $Q = \omega_0/\gamma$ where ω_0 is the angular frequency of the cavity mode and γ is the loss rate of photons from the cavity [59]. This means that a high loss of photons decrease the cavity's Q-value. The energy of a given cavity mode will decay according to the photon loss rate. Here absorption loss is neglected and only losses out of the cavity is considered. The energy decay for a given mode is expressed by:

$$U(t) = U(0) \exp\left(\frac{-\omega_0 t}{Q}\right) \tag{4.10}$$

where $U(t)$ is the energy stored in the cavity mode as a function of time t. Expressing the emitted power from the cavity by $P(t) = -dU(t)/dt$, the Q-value can be expressed by:

$$Q = \frac{\omega_0 U(t)}{P(t)} \tag{4.11}$$

For a 2D photonic crystal slab we consider light emitted into the vertical direction, perpendicular to the slab, and light emitted in directions in the plane of the slab. This can be expressed as:

$$Q_{\text{in}} = \frac{\omega_0 U(t)}{P_{\text{in}(t)}} \qquad \text{and} \qquad Q_{\text{v}} = \frac{\omega_0 U(t)}{P_{\text{v}}(t)} \tag{4.12}$$

The radiation loss in the vertical direction, is due to leaky modes. The radiation loss in the plane of the photonic crystal is due to a limited number of periods of the crystal lattice surrounding the cavity. The total emitted power $P = P_{\text{v}} + P_{\text{in}}$ and the total Q-value can be written as:

$$\frac{1}{Q} = \frac{P(t)}{\omega_0 U(t)} = \frac{P_{\text{v}}(t) + P_{\text{in}}(t)}{\omega_0 U(t)} = \frac{1}{Q_{\text{v}}} + \frac{1}{Q_{\text{in}}} \tag{4.13}$$

and thereby the total Q-value of the cavity is separated into a vertical and an in-plane Q. In order to obtain a desired performance it is important to note that equation (4.13) implies a certain condition on the in-plane Q_{in} and vertical Q_{v} [86].

4.2.2 Light emission from optical cavities

When dealing with 2D photonic crystal slabs loss may be caused by light scattered out of the plane of the crystal slab. This effect was exploited in order to achieve a drop functionality by introducing a single defect, where power is built up and then emitted in the vertical direction. This has been demonstrated experimentally in [87] where the defect is one hole with a larger radius than the bulk holes (acceptor-type defect). This cavity had a Q-value of $\sim$400. The tunability of the resonant frequency of this kind of defect by changing the defect radius has been investigated in [86] and was used as a drop filter, where the performance was optimized with respect to high output efficiency. This idea has been refined even further by introducing a donor type defect, where the defect is made by omitting one or more holes [88]. These kinds of defects are demonstrated to have Q-values of up to $\sim$6400 [89]. A component composed of an array of this type of defect structure, each designed to emit at different frequencies, was used to operate as a multiple channel drop filter [10]. Further development has focussed on improving the Q-value based on a design idea proposed in [90,91]. Using this approach a Q-value of $\sim$45000 was achieved [11].

All these designs have used out-of-plane emission of the trapped photons, which is not always suitable for integration of several drop components, since this would require multi-layer control or in- and out-coupling each time more components are put together resulting in too high coupling losses. Recently the same cavity as proposed in [11] was configured with an in-plane drop functionality by placing an output waveguide next to the cavity. They demonstrated Q-value of $\sim$13000 with an output efficiency of 65% [92].

Topology Optimized drop-filter

The structure presented in [92] consists of two line defect waveguides separated by 11 rows of holes with a cavity in between, formed by removing 3 holes along the waveguide direction. A similar configuration of the two waveguides and the central cavity was tested with the topology optimization. The design domain was defined around the cavity region. The structure is shown in figure 4.7. The input was positioned at the upper waveguide, depicted with a green arrow, and the transmission was detected at the lower waveguide, depicted by the blue area. The strategy was to maximize a wavelength at resonance in the cavity, and then minimize two neighboring wavelengths. By choosing the two neighboring wavelengths very close to each other the spectral output can in principle be made very narrow. Making a structure very sensitive to the wavelength, makes the optimization very sensitive to structural changes. Therefore it is extremely difficult to obtain an optimum solution with a high transmission and a narrow bandwidth simultaneously using this simple strategy and the present implementation of the program. More careful considerations are therefore necessary in order to make significant improvements to this design goal. In this work the investigation stopped at this preliminary stage, and it is a subject for future investigations.

Calculating the Q-value

By considering the light emitted from the cavity [86] or absorbed in the boundary of the cavity [59] it is possible to calculate the Q-value of a cavity resonator.

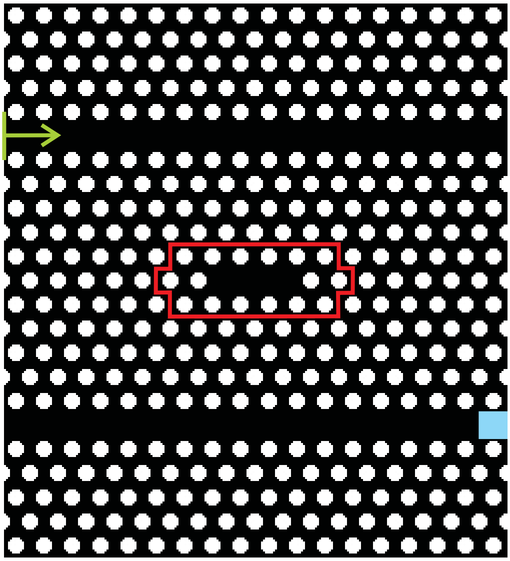

Figure 4.7: The initial structure used to optimize the functionality of an add-drop filter. The green arrow illustrates the incident wave. The design domain (Ω_D) is encircled by the red line. The Poynting-vector is maximized in the blue area (Ω_P) at the output port

In [93] an initial field having a large overlap with the defect mode is evolved in time by applying a FDTD scheme. The Q-value is then estimated from the the decay rate of the time evolution of the field in the cavity. A similar approach is used here, but is limited to consider the in-plane Q-value only. A 3D FDTD calculation of the decay rate is not possible with the used programme as it only allows for detectors to be placed perpendicular to the crystal plane, for detecting the in-plane propagation.

Decay calculations

The time evolvement of the fields can be simulated by the FDTD method, as described in section 3.3. The detectors store the field values at every time-step whereafter they can be plotted. Equation (4.10) relates the Q-value to decay rate of energy out of a cavity. The amplitude will decay as:

$$E(t) = E(0)\exp\left(\frac{-\omega_0 t}{2Q}\right) \tag{4.14}$$

and from this expression the Q-value can be evaluated as [94]:

$$Q = -\left[\frac{\omega_0(N_1 - N_2)\delta t}{2\ln(E_1/E_2)}\right] \tag{4.15}$$

where E_1 and E_2 are the field amplitudes at time-step N_1 and N_2, respectively, δt is the timestep given by equation (3.28).

The photonic crystal structure considered here had $\Lambda = 420$ nm and $D = 294$ nm. The grid size was $q_x = 0.01$ nm and $\delta t = 2.16 \cdot 10^{-11}$ μs. Figure 4.8 shows A) an isolated cavity formed by removing a single hole in a hexagonal photonic crystal lattice and B) the same cavity where a waveguide is formed by removing a row of holes. The cavity and the waveguide are separated by to rows of holes. The yellow and red lines, placed in the cavity, show a dipole-excitor and a detector, respectively. In a 2D FDTD simulation the considered structure had a bandgap 1.4–1.8 μm. The dipole-excitor emitted at 1600 nm, chosen to be in the middle of the bandgap, with a sinusoidal time-envelope of $N_{\text{env}} = 3000$, whereby the the wavelength range spanned the band of the photonic crystal. The detected field as a function of time from a 2D FDTD simulation is shown in figure 4.9 for the isolated cavity (upper part) and the cavity and a waveguide (lower part). As expected the field amplitude is seen to decay faster for the structure with the waveguide due to the coupling between the cavity mode and waveguide mode. Figure 4.10 shows the field amplitude as a function of time for a cavity and one waveguide (upper part) and a cavity between two similar waveguides (lower part). In this case the separation between the cavity and the waveguides was one row of holes. In the upper part it is seen that the decay of the field amplitude is faster, when there is only one row of holes separating the

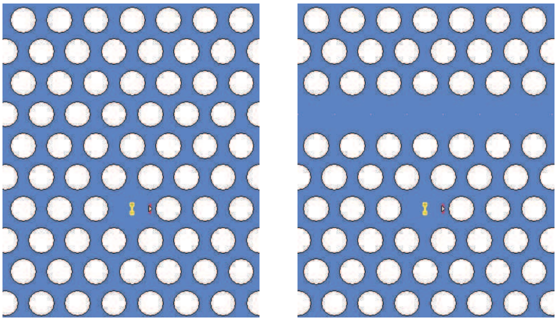

Figure 4.8: A) an isolated cavity formed by removing a single hole in a hexagonal photonic crystal lattice, with $\Lambda = 420$ nm and $D = 294$ nm, and B) the same cavity where a waveguide is formed by removing a row of holes. The cavity and the waveguide are separated by to rows of holes. The yellow and red lines, placed in the cavity, show a dipole-excitor and a detector, respectively.

cavity and the waveguide, when compared to figure 4.9, where there is a two hole separation. When comparing the upper and lower part in figure 4.10 it is also seen that the decay is further increased when the cavity is placed between two waveguides. The presence of the waveguides will introduce more resonant modes in the cavity. The field amplitudes in the figure show some rippling, which is expected to be caused by these cavity modes having different decay rates due to a different coupling to the waveguides. The normalized flux through the detector as a function of wavelength is shown in figure 4.11. In accordance with the rippling of the decay rates, in figure 4.10, it is seen that more resonance peaks show up when waveguides are added close to the cavity. To sustain a significant Q-value, the configuration with two rows of holes separating the cavity and the waveguides was used.

Drop filter

A single cavity, formed by simply removing one hole, between two waveguides, as described above, showed no actual drop performance when the upper input arm was excited, since the coupling to the cavity was observed to be very weak.

A simple cavity was proposed in [12] with a very high vertical Q-value and hence the total Q-value can essentially be determined by the in-plane Q-value alone, according to equation (4.13). The authors considered an isolated cavity, and in this work it was configured with two waveguides for in-plane coupling. In figure 4.12 is shown the field distribution of a cavity mode, A) for an isolated cavity and B) a cavity configured with two waveguides. The lower parts of the

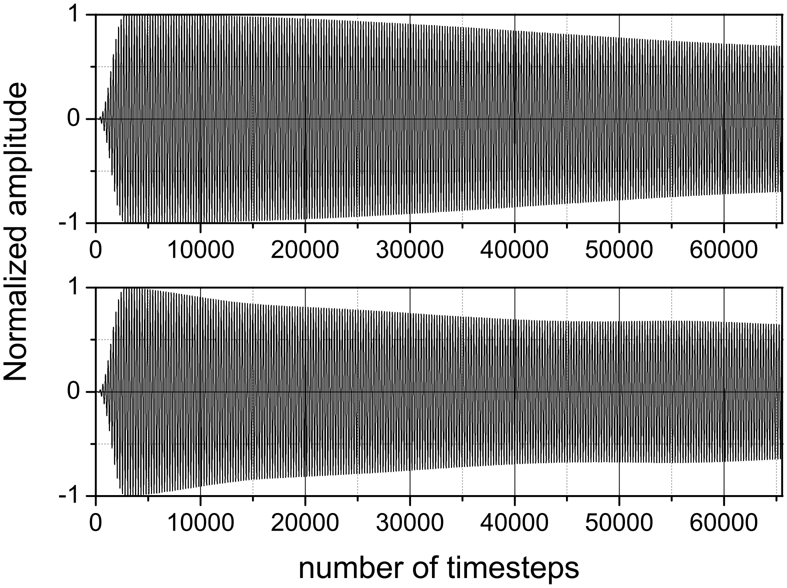

Figure 4.9: The field amplitude as a function of time step in A) a single cavity and B) a single cavity separated from a waveguide by two rows of holes.

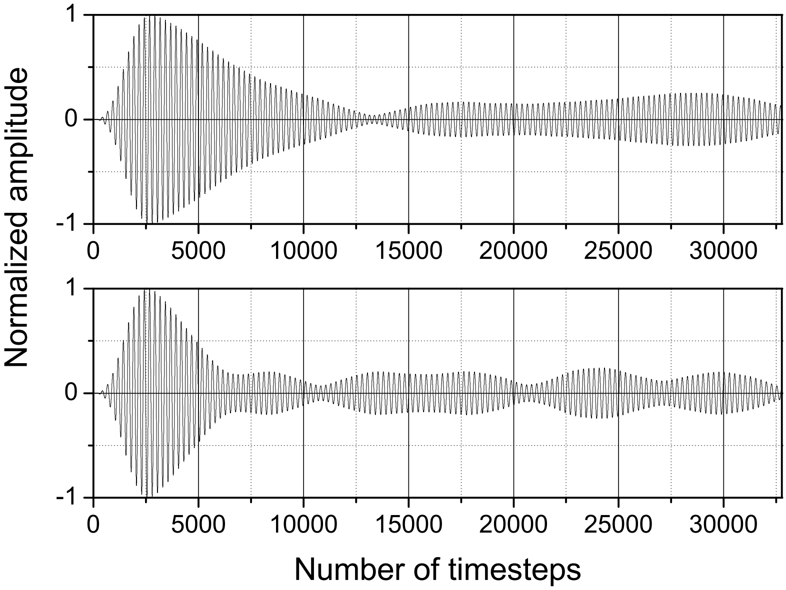

Figure 4.10: The field amplitude as a function of time step in A) a single cavity separated from one waveguide and B) two waveguides by one row of holes.

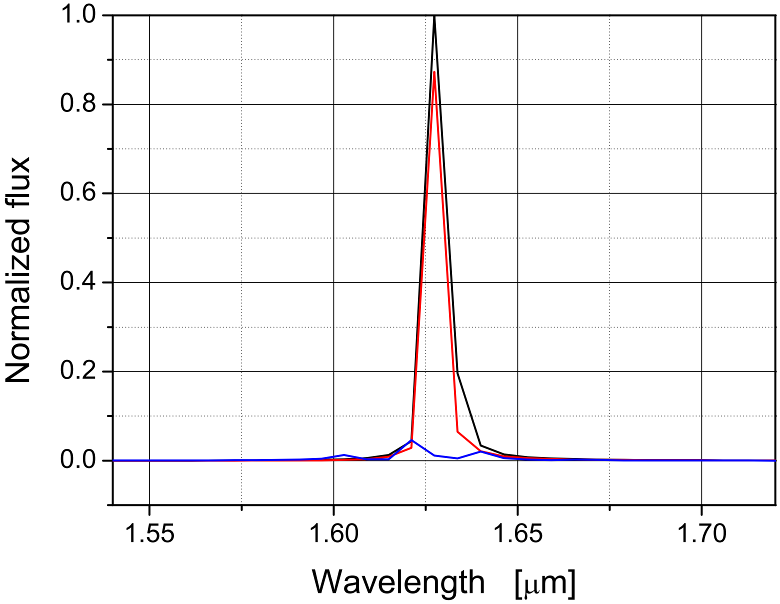

Figure 4.11: The normalized flux as a function of wavelength for a single isolated cavity (black curve), one waveguide added (red), and two waveguides added (blue).

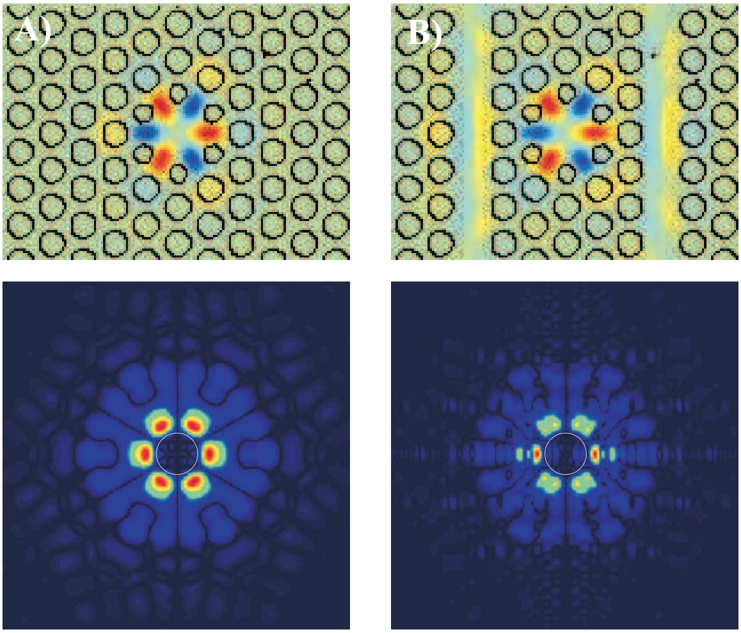

Figure 4.12: Field distributions of a cavity mode in A) isolated cavity and B) a cavity configured with two waveguides. The lower parts show the corresponding fourier transform of the field distributions. The white circle marks the light-cone.

figure show the fourier transform of the fields. By introducing the waveguides some of the fourier components inside the light cone grow slightly, marked with the white circle. This means that the mode is more leaky to out-of-plane emission [90, 91]. The same tendency is observed for other modes in the cavity as well. The complete structure is shown in the left part of figure 4.13. The holes closest to the cavity center have a radius of 218 nm and are shifted 38 nm out from the center. The naive idea was that this could perhaps provide a better coupling from the waveguide to the cavity, as the periodicity is broken.

The right part of figure 4.13 shows the steady state field distribution with the excitor placed in the cavity. The field distribution indicates that the mode in the cavity couples to the odd-mode of the waveguide.

The transmission at the drop port for an even and an odd excitation is shown in figure 4.14, and a slight increase in the dropped transmission is observed. Several modes exist in the proposed cavity. The high Q-value reported was for a specific mode, thus the Q-value depends strongly on the excitation of one specific mode, and it is not sufficient only to consider one mode as usually several modes

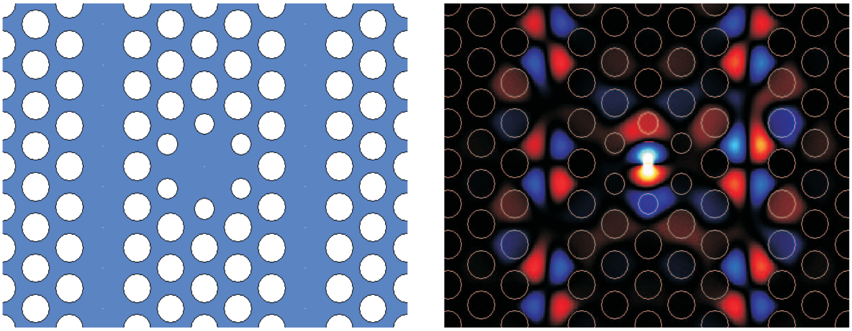

Figure 4.13: Left part: A cavity and two waveguides. The cavity and the waveguides are separated by one row of holes. The photonic crystal lattice has $\Lambda = 420$ nm and $D = 294$ nm. The holes closest to the cavity center have $D = 218$ nm and are shifted 38 nm out from the center. Right part: Steady state field distribution of the same structure calculated using 2D FDTD with the excitor placed in the cavity.

are excited unless special care is taken.

From the above consideration it is clear that this rather simple approach is not useful for designing a sufficiently good drop functionality. The approach can merely be used to gain some insight of the behavior of single cavities. The coupling issue is very essential and other methods are needed as pointed out in [95]. Furthermore the introduction of the waveguides leads to a slight increase in the out-of-plane loss and thereby a reduction of the Q-value.

4.2.3 Transmission filters

Another type of filter is the transmission filter, which is characterized by a narrow transmission bandwidth. A transmission filter is basically a single waveguide coupled to a single cavity. Such a filter consist of a photonic crystal waveguide where the cavity is formed in the waveguide. This type of structure is shown in figure 4.15, where the cavity element actually consists of two coupled cavities. The calculated transmission spectrum is shown in figure 4.16.

It is seen that the transmission shows narrow peaks with almost full transmission. By carefully designing the positions of the holes in the cavity it is possible to optimize the performance of the filter [9]. A conventional add-drop multiplexer is configured with 3 dB couplers and bragg gratings [96]. The bragg gratings provide the wavelength selectivity in reflection. In analogy to this, it would be interesting to investigate the possibility to combine the transmission filter with 3 dB couplers, which has already been demonstrated [8]. In this case

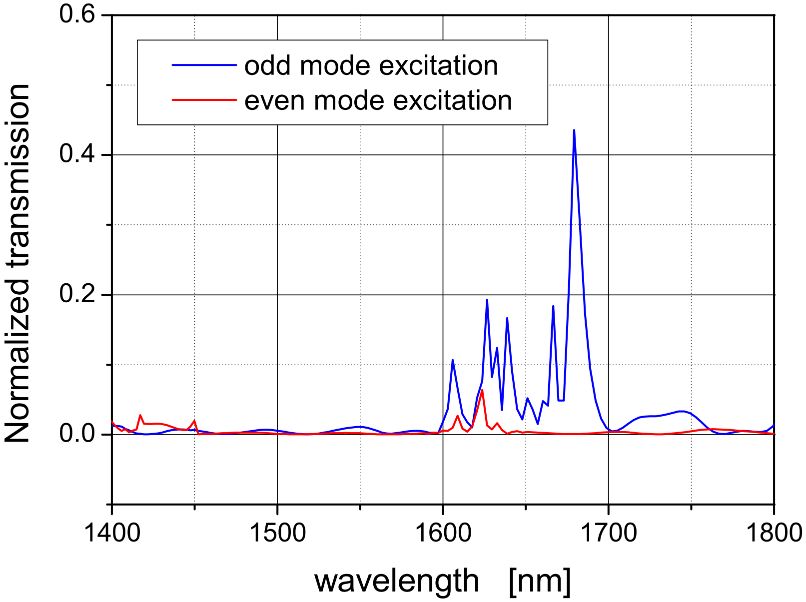

Figure 4.14: Transmission spectrum at the drop port for an even and an odd excitation of the waveguide at the input port.

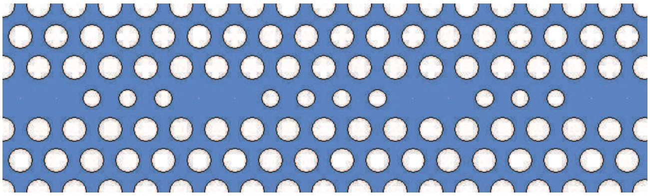

Figure 4.15: Transmission filter consisting of a photonic crystal waveguide where the cavity is formed in the waveguide.

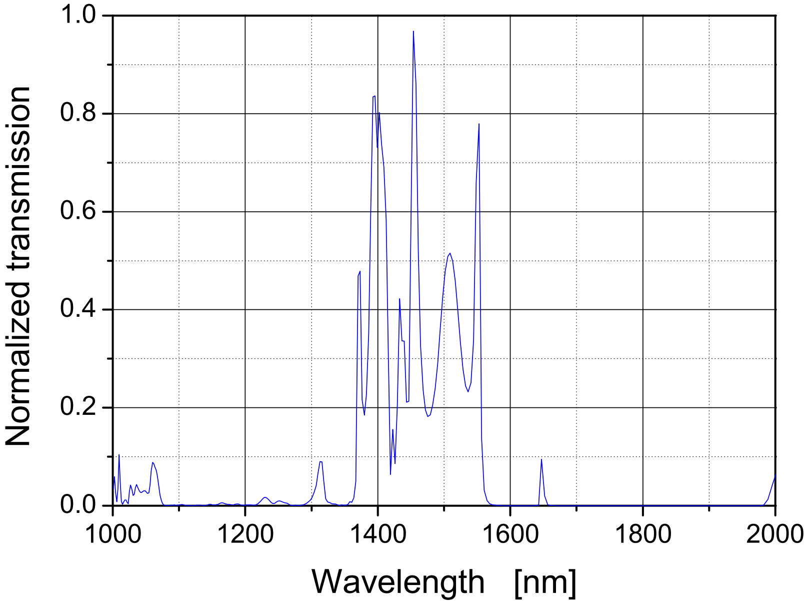

Figure 4.16: Transmission calculation of the transmission filter shown in figure 4.15.

the wavelength selectivity is provided in transmission instead of reflection. This would of course require optimization of both the coupler and the transmission filter. It is a obvious task to optimize the coupler using topology optimization and these issues may be covered in future work.

This chapter has dealt with different issues for designing components concerning the optimization of a desired performance. Topology optimization have proven to be very suitable for achieving high transmission in a very large bandwidth for simple components. For narrow band functionalities some more careful considerations have to be carried out in order to apply this method. Other attempts to get an understanding of these kinds of functionalities have been presented, but it is a complex and challenging task, and a lot of issues need to be investigated further.

Chapter 5

Fabrication and Characterization

This chapter deals with the experimental issues ranging from fabricating the photonic crystal components according to some design specification, to the final characterization in order to evaluate how the components perform compared with theoretical expectations. The fabrication involves several delicate processes as high resolution patterning, using e-beam lithography or Deep UV (DUV) lithography, followed by an etching process, for transferring the patterns into the material, and finally the cleaving of the samples into smaller pieces. When the samples have been fabricated they are spectrally characterized by optical transmission measurements. This chapter is divided into three main sections concerning the fabrication, the characterization of the photonic crystal components, and finally a discussion of the obtained results.

5.1 Fabrication

As described in chapter 2 the material choice in this work is a silicon-on-insulator (SOI) substrate. Therefore the photonic crystal structures considered in the previous chapters all had material properties corresponding to a silicon core layer with air-holes. The obtained design, as described in chapter 4, should now be transferred into the SOI substrate. The fabrication procedure consists basically of the following fabrication steps:

1. Resist spinning and baking of resist
2. Lithographic process
3. Development and post-baking of resist

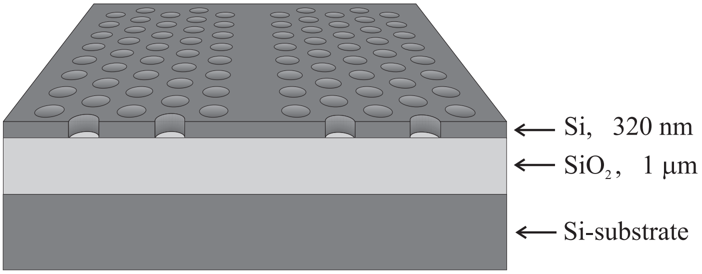

Figure 5.1: A schematic illustration of a typical photonic crystal structure consisting of three layers. The thin upper Si-layer is used as the guiding layer and contains the photonic crystal waveguide.

4. Etching process and resist stripping

5. Cleaving of the processed sample into smaller pieces for the final characterization

A generic photonic crystal waveguide is shown in figure 5.1. A more detailed description on the different fabrication steps is given in the following.

5.1.1 Lithography

The lithographic process is very demanding in order to make photonic crystals operational at the telecommunication wavelengths. A very high resolution is needed to satisfactorily produce the crystals which have feature sizes as small ∼200–400 nm. In standard optical lithography a way to decrease the smallest obtainable feature size is to use a smaller wavelength. A lot of work have been done on developing a lithographic process using a wavelength in the Deep UV at $\lambda = 248$ nm. The use of Deep UV lithography involves advanced dedicated equipment and the process involves several complicated process steps. The work on Deep UV lithography have been performed by coworkers as a part of the 1st European PICCO project. Further details can be found in [97,98]. Most of the previous samples was fabricated using this method.

Recently a e-beam facility became available at Danchip, DTU and the most recent samples used in this work were therefore fabricated using a e-beam lithographic process.

Electron beam lithography

In usual optical lithographic processes the whole pattern covers up to a full 8" wafer, which is exposed at once. In an e-beam lithographic process a single focussed electron beam is scanned across a sample coated with an electron sensitive resist. Thereby the written pattern is transferred into the resist. The e-beam technique is therefore a slower process, due to the serial way of transferring the pattern. This method, however, shows great advantages since the smallest obtainable feature size is not limited by diffraction as the wavelength of high energy electrons is exceedingly small [36]. Hence very high resolution lithography can be obtained. For research and development purposes the e-beam lithography technique is extremely useful.

Resist The used resist-type is *ZEP-520*[1] which is a very high resolution positive resist with a high sensitivity. The exposure of the resist to electrons causes bond breakage leading to a higher solubility, whereby the exposed areas are easily removed in a developing process. A great advantage of this resist is that it has a high resistance to dry etching techniques.

To provide a better adhesion of the resist to the substrate, the samples are cleaned in acetone, methanol, and isopropanol and blown dry in nitrogen prior to the resist spinning. The resist is contained in a liquid solvent and a few drops of the resist is applied to the wafer. The wafer is fixed by a vacuum chuck on a resist spinner, which is subsequently started with a preset spinning speed and time, resulting in a thin film of resist covering the wafer. For spinning speeds at 2000–6000 rpm the resist thickness is in the range 300–500 nm. Diluting the resist with anisole results in a thinner resist film. For a 1:1 solution the thickness is in the range 100–200 nm [99].

Several limitations such as adhesion and resolution, become less severe when the resist thickness is decreased. But still a sufficient thickness of the film is necessary in order to maintain enough resistance to the etching procedure.

From earlier experience a good choice is to use a 1:1 dilution of the resist in anisole and to spin at a speed of 6000 rpm for 1 minute. Hereafter the samples were baked on a hotplate at 185°C for 3 minutes to drive out the solvents and harden the resist film [100].

Design files The input to the e-beam facility is a specific type of file called a GDS-II file. The GDS-II file format is binary and supports a hierarchical structure of layers that may contain a number of geometrical objects as polygons and boxes. Different layers typically represent different processing steps for exposure [101]. Through specialized software products such as *L-edit*[2] and

---

[1] *http://www.zeon.co.jp/business_e/enterprise/imagelec/imagelec.html#ie1-1*

[2] http://www.tanner.com/EDA/products/ledit/default.htm

Elphy-Plus[3] the desired design can be drawn and exported as a GDS-II file and then transferred to the control computer of the e-beam facility. Beside the actual photonic crystal components, the design file contains long ridge waveguides leading to and from the photonic crystal component in order to be able to couple light from silica fibers into the photonic crystal, see section 5.2.1. The ridge waveguides typically have lengths of ∼3–4 mm and are, from the photonic crystal, tapered from a width of 1 μm to 4 μm over a distance of 150 μm. An example of a layout is shown in figure 5.2. The colored areas correspond to areas exposed to the electron beam. Exposed areas are removed in the development process and therefore the ridge waveguides are defined by exposing the areas surrounding the waveguide core, extending ∼4–10 μm from the waveguide edge. The ridge waveguides and the photonic crystal structure are placed in separate layers as illustrated with different colors (blue and green), and thereby it is possible to apply different e-beam exposure doses to different parts of the design. This is quite important in order to obtain good result when the design file contains dissimilar structures with different demands on the dose.

Electron exposure The used equipment is a JBX-9300FS Electron Beam Lithography System from the company *JEOL*[4] featuring a spot beam, vector scan, and a step and repeat stage. By the vector scan strategy the complete pattern is divided into smaller fields. Each field is written at a time and the stage moves from field to field and thereby stitching together the full pattern. The writing field has a size of 500×500 μm and by careful calibration the stitching error is below 30 nm. The mounting facilities in the e-beam at the time of use were limited to handle 2" wafers. By cleaving a 4" wafer into pieces of 5×1 cm the pieces could be fitted into the 2" sample-mount. The used settings of the e-beam machine were an acceleration voltage of 50 kV and a beam current of 1 nA.

After the exposure the sample was developed in ZED-N50 (n-Amyl acetate) for 1 minute, rinsed in ZMD-B (89 % Methyl Isobutyl ketone Isopropyl alcohol) for 20 seconds, and blown dry with nitrogen. The resist was subsequently post-baked at 130°C for 3 minutes.

Proximity effects caused by electrons, which are scattered on impact with either the resist or the substrate, result in unintended exposure of areas close to the position of the beam incidence and have a great influence on the fine details of a written pattern. When large adjoining areas or areas with closely spaced structures have to be exposed, the proximity effects are more pronounced, as the beam spend more time in such areas. An example of this effect is seen in figure 5.3. The figure shows SEM images of samples that were written with different exposure doses, and subsequently developed. The images show the

---

[3] http://www.raith.com/WWW_RAITH/nanolithography/nano_elphyplus.html

[4] http://www.jeol.com/eb/eblprods/jbx9300fs.html

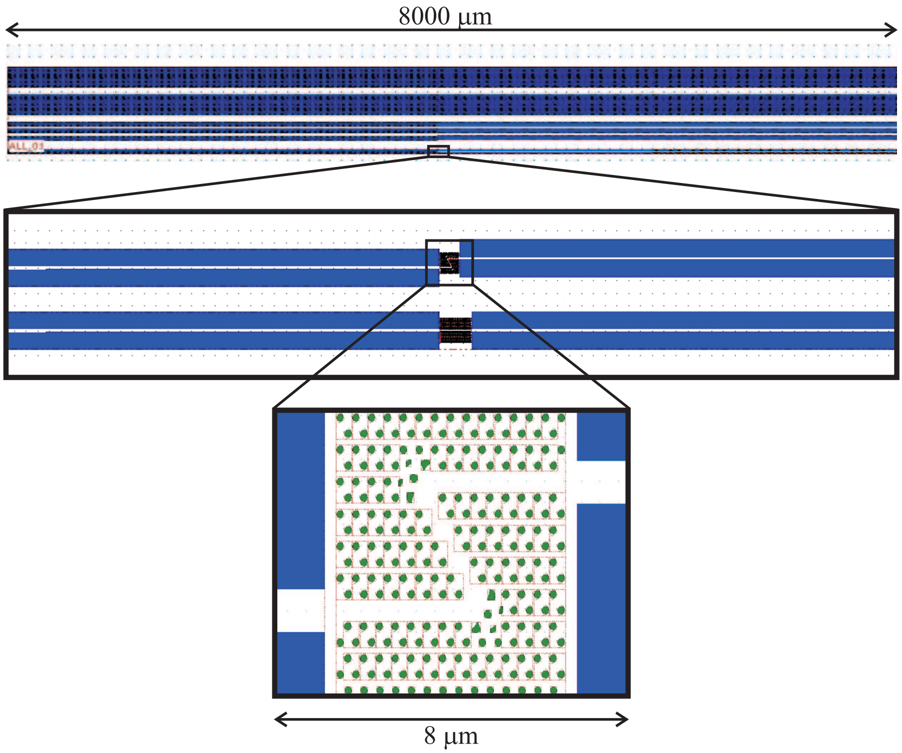

Figure 5.2: Example of a typical design file. The design contains long ridge waveguides (blue areas) leading to and from the photonic crystal component (green), shown enlarged in the lower part of the figure. The total length of the ridge waveguide and component is typically around 8 mm.

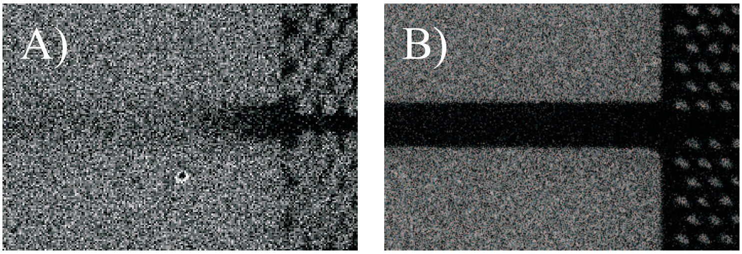

Figure 5.3: SEM images of samples that were written with different exposure doses, and subsequently developed. The images show the transition region between the ridge waveguide and the photonic crystal. In part A) the core of the ridge waveguide is clearly seen to be over-exposed. In part B) the dose is decreased and the waveguide core is clearly distinct, but the holes of the photonic crystal are slightly under-exposed

transition region between the ridge waveguide and the photonic crystal. In part A) the core of the ridge waveguide is clearly seen to be over-exposed. In part B) the dose is decreased and the waveguide core is clearly distinct, but the holes of the photonic crystal are slightly under-exposed. To comply with this, it was therefore necessary to adjust the exposure dose for the ridge waveguides relative to the exposure dose of the holes in the photonic crystal. Good results were obtained by writing the ridge waveguides with half the dose used for the holes. All the following structures were written with these settings. No further proximity corrections were applied.

Due to imperfect filament conditions, the beam was slightly out of focus, and the beam width was ~50 nm. Corrections to compensate for this deficiency were undertaken by appropriate modifications of the design files. To take into consideration the experimental deviation of the fabricated structures from the intended design, each design was written several times using different exposure doses. The used doses were 125,150,175 μC/cm^2.

5.1.2 Reactive ion etch

After the e-beam exposure and subsequent development, the written patterns were transferred into the top silicon layer of the SOI substrate by an anisotropic reactive ion etch (RIE). The RIE process is a dry etching technique, which provides a good reproducibility and control of the etch profile [102]. The RIE process is carried out in a reaction chamber containing two horizontal plate electrodes opposing each other. The top electrode is connected to ground potential and is constructed as a showerhead for distributing the inlet gases evenly. The

Parameter	Value	Unit
SF_6 flow	32	sccm
O_2 flow	8	sccm
Pressure	80	mTorr
Power	30	W

Table 5.1: The deposition parameters used in the RIE process. The process was optimized for high anisotropy

sample is placed on the bottom electrode, which is connected to a RF-power generator through a blocking capacitor. By applying a RF power signal to the electrode a plasma is created from ionization and dissociation of the inlet gases. The etchant used here is fluor which is primarily formed from the inlet gas SF_6 according to the reaction:

$$e^- + \mathrm{SF}_6 \longrightarrow \mathrm{SF}_5 + \mathrm{F} + e^- \tag{5.1}$$

The silicon surface is chemically etched by the fluor atoms as they diffuse to the silicon surface and by the chemical reaction:

$$\mathrm{Si} + 4\mathrm{F} \longrightarrow \mathrm{SiF}_4 \tag{5.2}$$

forms a volatile product that is pumped away. This etch mechanism is in its nature isotropic as all exposed areas will etch at the same rate. To achieve anisotropy oxygen is added to the plasma. Oxygen will compete with F for sites on the silicon surface, forming a passivating layer of oxy-fluorides which will inhibit the reaction between silicon and fluor to occur. However this inhibition will only persist on the sidewalls as the oxy-fluorides on the horizontal surfaces will be removed by the bombardment of ions in the plasma, and thereby expose silicon to the fluor atoms. This way the removal of silicon only takes place at the horizontal surfaces. By adding the right amount of oxygen, the etch profile can to some extend be tailored. In practice the variable parameters in a RIE process are gas-flow, gas composition, chamber pressure and RF power. The used process was optimized for high anisotropy and high etch rate uniformity in both silicon and poly-silicon as reported in [24, 40]. The etching process parameters are listed in table 5.1. Significant day-to-day variations in the etch depth as a function of time have been observed. The resist is rather thin and it is very important not to etch through the resist, as this would result in a considerable roughening of the surface. Therefore etch tests in order to adjust the etch time are performed on dummy samples prior to etching the real samples. This includes measuring the resist thickness and silicon etch depth for different etch times to make sure to etch all the way through the silicon, without etching through the resist. The resist thickness and silicon etch depth are measured with a DEKTAK-profiler[5] with a resolution down to 1–2 nm.

The etching process was optimized for good selectivity for both Si:SiO$_2$ and Si:Resist and high anisotropy at a mask coverage of 40–60 % of a 4" wafer [103]. Increasing the exposed silicon area will not make any significant change of the anisotropy in a silicon etch. If on the other hand there is a decrease in the exposed area then there will be an overload of fluor eventually resulting in an isotropic etch [104]. The written structures considered in this thesis generally only occupy a very small area and are therefore placed on a standard silicon wafer in order to increase the exposed silicon area. After the silicon etch, the resist residuals are stripped using a oxygen rich plasma. The fabrication steps are schematically sketched in figure 5.4.

The fabricated samples are inspected in a SEM to check for defects which have arisen from the fabrication processes and to measure the characteristic dimensions of the fabricated structures such as hole-diameters and the lattice pitch of the photonic crystal. Figure 5.5 shows the fabricated hole size as a function of the designed hole size for three different lattice pitches. It is seen that the deviation depends on the lattice pitch of the photonic crystal. It is important to know the deviation between the designed and the actual fabricated structure so that it can be taken into account in the next iteration of component development, in order to be able to fabricate components with an accurately predetermined performance.

Cleaving

In order to be able to access the ridge waveguides from the facets the samples have to be cleaved. The position of the cleavage is specified by a 2–3 mm long scratch made on both sides of the sample with a diamond tip, and it can be controlled within 100–200 μm accuracy. The final samples have usually widths of 4–8 mm and are often quite difficult to cleave since the cleavage not always follows a specific crystal direction for such small samples. Hence the facet may become curved. In worst case the curved facet crosses into the photonic crystal or points where the ridge waveguide is tapered down to a narrow width and thereby deteriorating the coupling from the fibers dramatically. The ridge waveguide are therefore made relatively long to avoid this concern.

5.2 Characterization

The characterization of the fabricated components is basically a matter of measuring how they respond to a given optical input and thereby evaluate the component performance according to the expectations obtained from theoretical

---

[5] http://www.veeco.com/

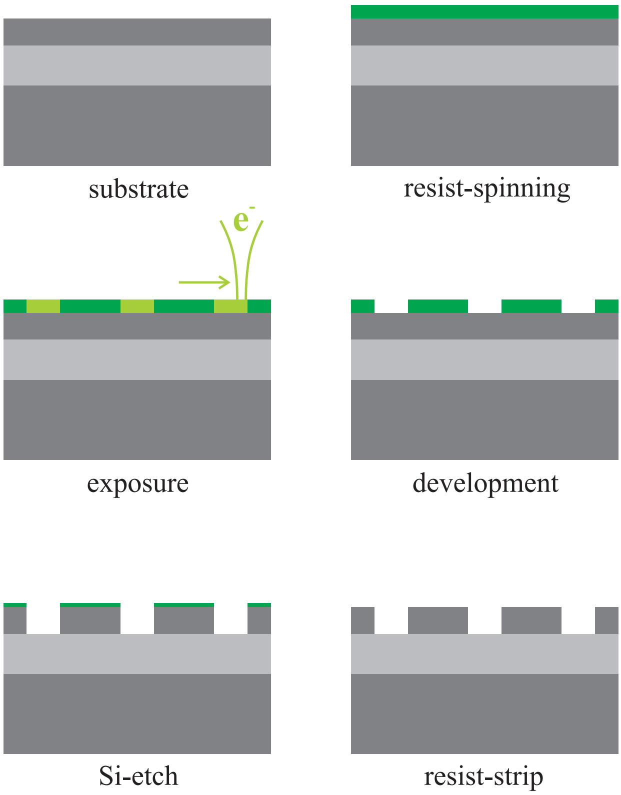

substrate

resist-spinning

exposure

development

Si-etch

resist-strip

Figure 5.4: Schematic illustration of the process steps of the fabrication of photonic crystal components

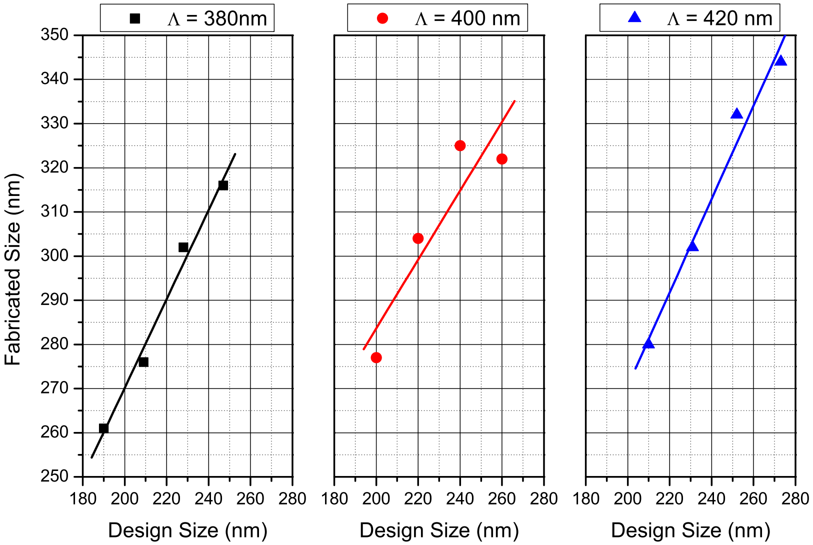

Figure 5.5: Graphs showing the experimentally determined hole size as a function of the designed hole size for three different lattice pitches

simulations. The setup and experimental procedure are outlined in the following.

5.2.1 Characterization setup

The setup used for the characterization of the fabricated photonic crystal components is schematically shown in figure 5.6. From the light source the signal propagates through a polarization controller, a polarizer, another polarization controller into a tapered lensed fiber aligned to the input position of the sample. From the tapered lensed fiber the light is coupled into the sample, propagates through the sample, and is coupled out into a similar tapered lensed fiber aligned to the output position. The light then propagates to an optical spectrum analyzer (OSA) that detects the transmitted power as a function of wavelength.

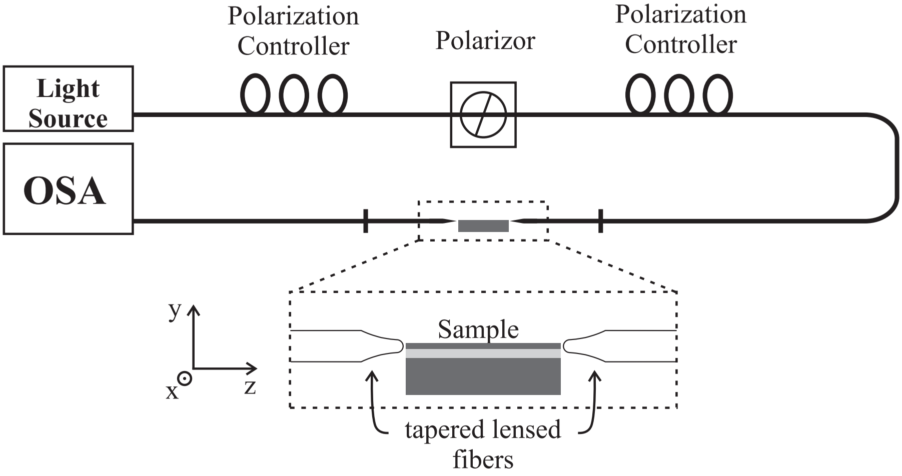

Figure 5.6: The setup used for the characterization of the photonic crystal components. From the light source the signal propagates through a polarization controller, a polarizer, another polarization controller into a tapered lensed fiber aligned to the input position of the sample. From the tapered lensed fiber the light is coupled into the sample, propagate through the sample, and is coupled out, into a similar tapered lensed fiber aligned to the output position. The light then propagates to an optical spectrum analyzer (OSA) that detects the transmitted power as a function of wavelength.

A vacuum chuck fix the sample on a translational stage placed under an optical microscope for visual inspection of the sample and coarse positioning relative to the input and output fibers. The fibers are placed on three-axis translational stages with sub-micron precision whereby the fibers can be aligned very accurately to the sample for maximum in-coupling and out-coupling. The tapered lensed fibers focus the light down to a spot-size of $\sim$3 μm and thereby provide a higher coupling efficiency to the high index ridge waveguides. Optimum coupling is achieved at a finite distance between the fiber tip and the sample due the finite focal length of the fiber, and thereby no special attention for accidentally crashing the fiber into the sample is needed. Alignment of the fibers to the sample is done by maximizing the transmission through the sample at a given wavelength, preferably at a wavelength with high throughput power.

The light source is either a light emitting diode (LED) or tunable laser source (TLS) depending on which properties of the photonic crystal that are investigated. The LED is a broad band source with two diodes emitting at wavelengths peaking around 1322 and 1538 nm, respectively. The LED source is used for broadband transmission measurements, and a single spectrum covering a wavelength range 1100–1700 nm can be recorded. The TLS has a narrow bandwidth with a output power level of >2 $\mathrm{dB_m}$ in the tuning range from 1520–1620 nm or 1480–1580 nm. The TLS is used for narrow-band investigations, where fine details in a spectrum are investigated.

It is very important to have a precise knowledge about the polarization of the light, as this has a great influence on the propagation properties of the photonic crystal components. A sample containing ridge waveguides showing a $\sim$20 dB higher transmission for TE- compared to TM-polarization is used. This sample has a rather thin upper silicon layer and is expected to cause mode cut-off for the TM-polarized light. The light from the polarizer passes through the polarization controller before reaching the sample. By maximizing the transmission using the polarization controller the TE-polarization is obtained. The TM-polarization is obtained by turning the polarizer 90°.

This method is in agreement with a more thorough determination method, carried out for the used setup, using a Glan-Thomson polarizer, which has a high extinction ratio between two perpendicular linear polarizations in a large bandwidth, whereby the two polarizations can be clearly distinct [105].

The first polarization controller is optional but is used to achieve a higher throughput power when using the LED source. Since the LED source is partially polarized a $\sim$1 dB increase of power can be obtained by adjusting the polarization controller for a given orientation of the polarizer.

By applying the above mentioned procedure several photonic crystal components have been characterized. The most important results are presented in the next section.

5.3 Results and Discussion

The results obtained from the fabrication and characterization procedures will be presented below. Several types of photonic crystal components have been fabricated and characterized.

Straight waveguide

As an illustrative example the calculated and measured transmission for TE-polarized light through a straight photonic crystal waveguide is shown in figure 5.7. The transmission has been normalized to the transmission spectrum for a ridge waveguide located on the same sample. The inset shows a scanning electron microscope (SEM) image of the fabricated structure. The photonic crystal waveguide has a total length of ∼10 μm. The diameter of the holes is $D = 0.76\Lambda$ where $\Lambda = 428$ nm is the lattice pitch. This example illustrates a very characteristic feature of a photonic crystal waveguide namely the marked drop in transmission when the wavelength is outside the transmission bandwidth of the guided mode in the bandgap. It is evident that the 3D FDTD calculations successfully explain all essential features of the spectrum as well as the actual transmission level. The position of the sharp cut-off around 1540 nm is in excellent agreement with previous band gap calculations. The small frequency shift (approximately 1–2%) between the experimental and simulated spectra is due to uncertainties of the experimental parameters and the limited grid resolution of the 3D FDTD calculations. For wavelengths longer than 1540 nm the measured transmission appears to be less suppressed than the calculated one. This is due to the fact that experimentally it is not possible to completely extinguish the TM polarization. In [106] it was found that TM polarized light propagates with very low loss in straight photonic crystal waveguide in this wavelength range. Hence, the measured transmission will unavoidably include a small part of TM polarized light, and this small TM contribution plays a rather significant role at the longer wavelengths, where there are no guided TE-polarized modes in the photonic crystal waveguide. The calculations, however, are performed utilizing a purely TE polarized light source.

Topology optimized z-bend

As described in chapter 4, a novel design method called topology optimization has been applied to a simple photonic crystal z-bend and a significantly improved performance was achieved. The improved design also showed very convincing performance in 2D and 3D FDTD simulations. Such a structure has been fabricated and characterized. A SEM image of the fabricated z-bend is shown in figure 5.8. The fabricated z-bend has a lattice constant $\Lambda = 430$ nm, by this choice the spectral features of interest lies in the telecommunication window. The

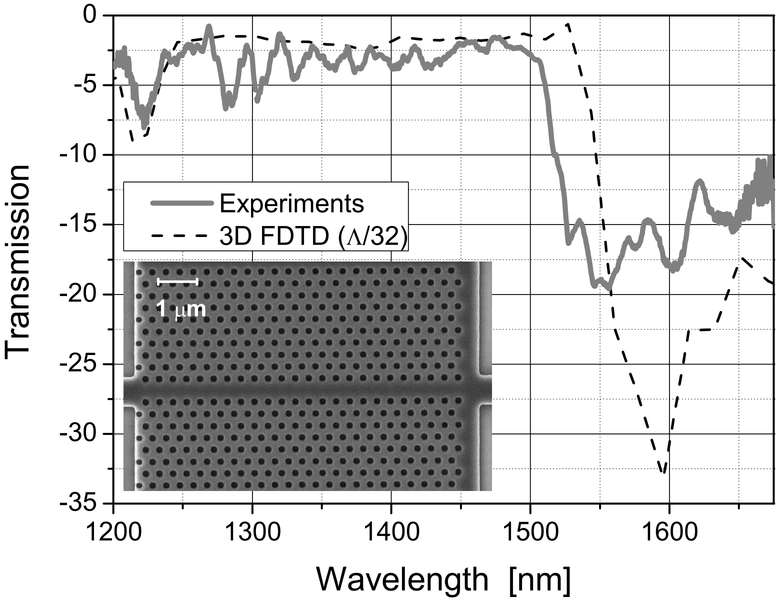

Figure 5.7: Measured (gray) and calculated (dashed black) transmission spectra for a 10 μm long waveguide. The transmission has been normalized to the transmission spectrum for a ridge waveguide located on the same sample. The inset shows a SEM image of the fabricated structure.

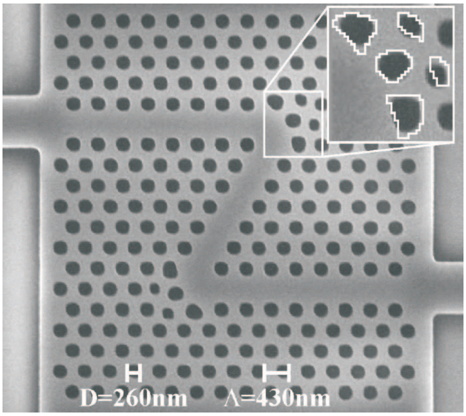

Figure 5.8: A SEM image showing the fabricated z-bend described earlier. The number, shape and size of the holes at each bend are designed using topology optimization. The inset shows a magnified view of the optimized holes as designed (white contour lines) and actually fabricated.

regular holes have a diameter $D = 260$ nm. Thereby the ratio is $D/\Lambda = 0.60$, which is close to the designed ratio of $D/\Lambda = 0.58$. Due to the finite e-beam size the fabricated structure deviates from the optimized design. The inset of the figure shows a contour plot of the designed hole structure overlayed on the fabricated structure. The measured and calculated bend loss per bend is shown in figure 5.9. The spectra have been normalized to transmission spectra for straight photonic crystal waveguides of the same length. The calculation was performed on a structure similar to the fabricated one. The calculated spectrum displays good agreement with the experimental one, both regarding the bend loss level and the prominent features. The measured and calculated spectra appear to be shifted 1–2 % with respect to each other. This shift falls well inside the experimental uncertainty of the physical parameters and the uncertainty caused by the limited resolution of the grid spacing employed in the calculations. The most prominent feature of these spectra is the extremely broad wavelength range of more than 200 nm having a very low bend loss of 1 dB.

The topology optimization method has been employed for designing other type of photonic crystal components. These include a 60 degree bend, 90 degree bend, and a splitter which are briefly presented below.

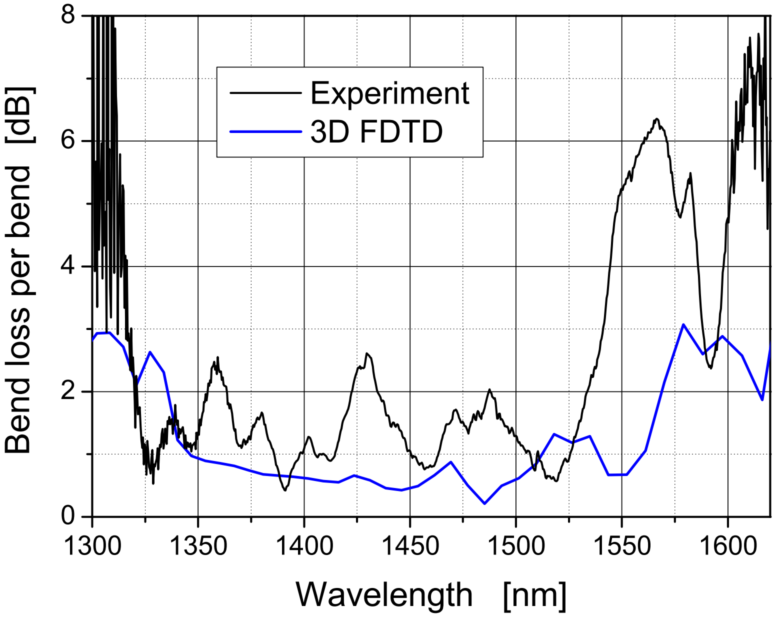

Figure 5.9: The measured (black) and 3D FDTD calculated (blue) loss per bend for TE polarized light in the fabricated structure.

60 and 90 degree bends and a splitter

In the following are shown the most recent results from the topology optimization. The fabrication has been performed in collaboration with Lars Hagedorn Frandsen, who did the characterization. A SEM image and a transmission measurement for each of the structures are shown below. The transmission through the components was measured for TE-polarized light using the LED sources. The spectra were recorded with a spectral resolution of 10nm using an OSA. To extract the loss through the components the transmission spectra have been normalized to the transmission spectrum for a straight photonic crystal waveguide of the same length, located on the same sample.

Figure 5.10 and 5.11 shows SEM images and the measured transmissions, respectively, for a topology optimized double 60 degree bend and the simple (un-optimized) structure. The 60 degree bend have an average bend loss of 0.43 ± 0.27 dB. In the same wavelength range the un-optimized bend clearly shows a large bend loss, which only reduces in a narrow range near the cut-off of the fundamental mode at longer wavelengths.

Figure 5.12 and 5.13 shows SEM images and the measured transmissions, respectively, for a topology optimized double 90 degree bend and the simple (un-optimized) structure. The 90 degree bend have an average bend loss of 0.74 ± 0.18 dB, and again the un-optimized bend show a significant higher bend loss.

It is interesting to note that the optimized bends have been smoothened by applying a soft curvature in the bend regions, resembling more the conventional strip type waveguide. However, the smoothening is not trivial as the design domain still contains complex structures. This is contrary to the optimized z-bend structure which still have structural features more similar to a regular photonic crystal. One could speculate that this agrees well with the more reflective functionality of a z-bend, compared to the 60 and 90 degree bend, since photonic crystals show high reflectivity for wavelengths in the bandgap [60].

In figure 5.14 and 5.15 is shown a SEM image and the measured transmission for a structure consisting of a topology optimized splitter followed by two topology optimized 60 degree bends. The topology optimized splitter displays smooth, low-loss, and nearly indistinguishable transmission spectra for the two output ports. The complete component is experimentally found to have a 100nm bandwidth with an average loss of 0.44 ± 0.29 dB. This value includes both excess losses due to the splitting region and the subsequent 60 degree bend. Also shown is the performance of a previously reported low-loss splitter [72] designed using intuitive design ideas. In contrast to the topology optimized splitter, the spectrum for the intuitive splitter is seen to be rather spiky, indicating resonant and high-loss behavior often observed for photonic crystal components. For the topology optimized splitter complex structures is again observed, emphasizing the non-triviality of the optimized structures.

The topology optimized components show a superior performance when com-

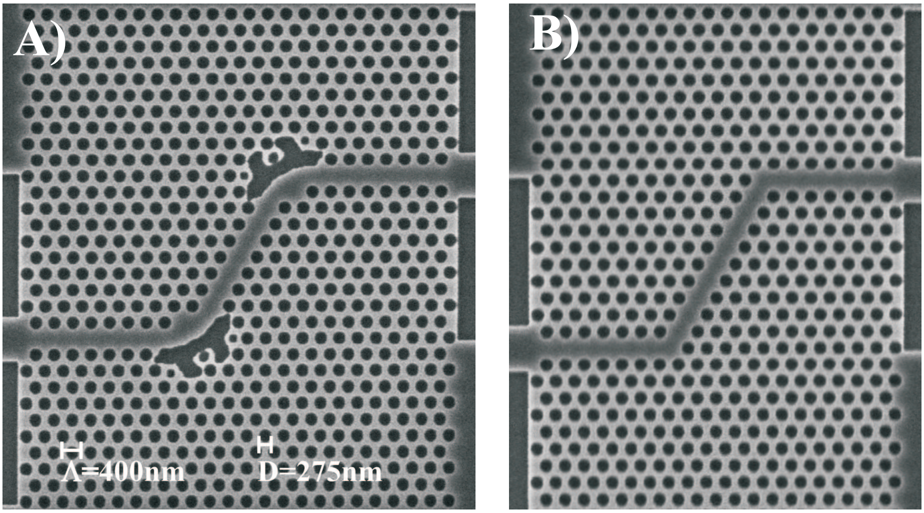

Figure 5.10: SEM images of the fabricated photonic crystal waveguides containing two consecutive 60 degree bends. The pitch of the triangular lattice is $\Lambda = 400$ nm with hole diameter $D = 275$ nm. A) waveguide with topology-optimized bends. The number, shape and size of the holes at each bend are designed using topology optimization. B) waveguide with simple (un-optimized) bends.

pared to the simple ones. The performance is characterized by a very low bend loss for the bends and very low transmission loss for the splitter in a large wavelength range. More details on these structures have recently been published and can be found in [107–109].

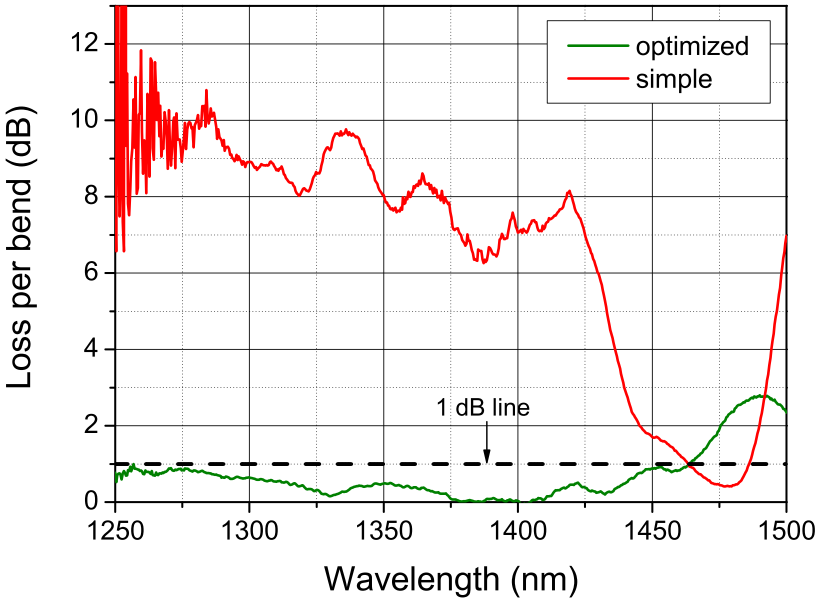

Figure 5.11: Measured loss per bend for the un-optimized 60 degree bend (red) and the topology optimized 60 degree bend (green). Both spectra have been normalized to the transmission through straight photonic crystal waveguide of the same length to eliminate the coupling and the propagation loss in straight waveguides. The dashed line marks a bend loss of 1 dB.

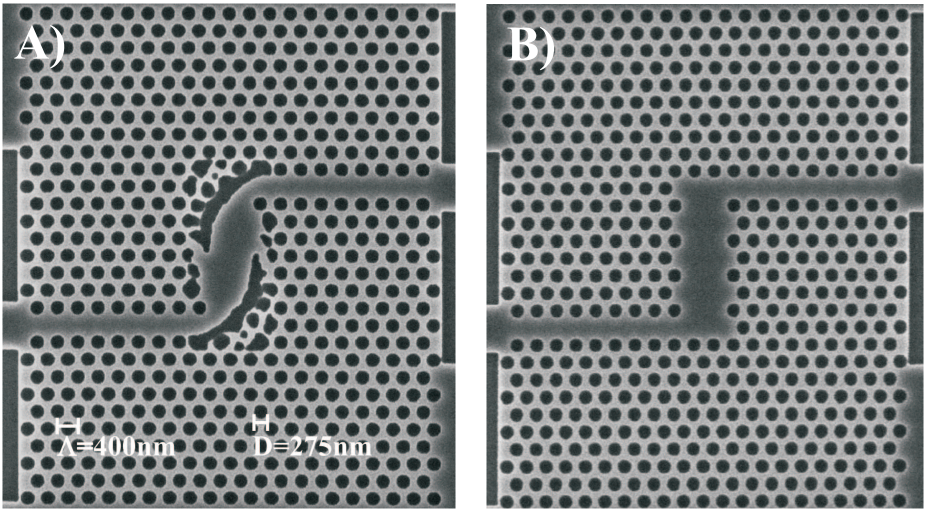

Figure 5.12: SEM images of the fabricated photonic crystal waveguides containing two consecutive 90 degree bends. The pitch of the triangular lattice is $\Lambda = 400$ nm with hole diameter $D = 275$ nm. A) Waveguide with topology optimized bends. The number, shape and size of the holes at each bend are designed using topology optimization. B) Waveguide with simple (un-optimized) bends.

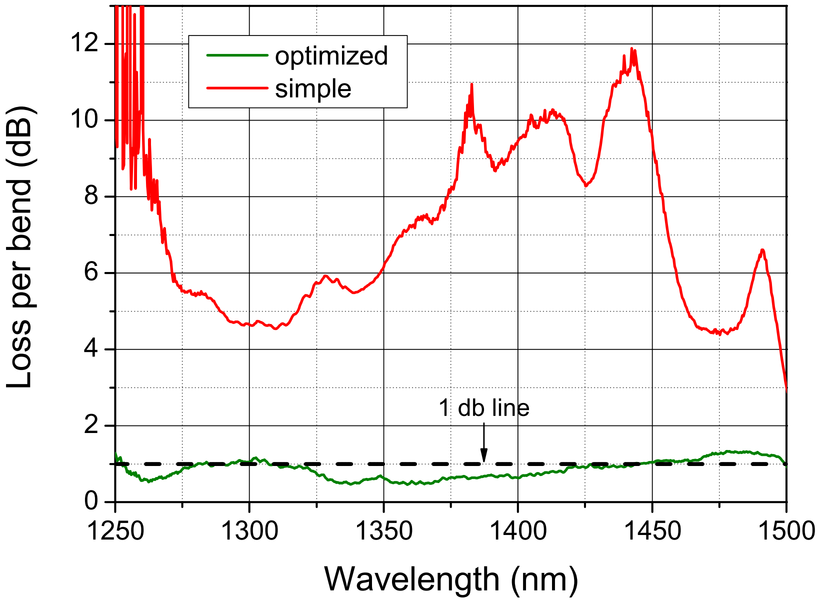

Figure 5.13: Measured loss per bend for the un-optimized 90 degree bend (red) and the topology optimized 90 degree bend (green). Both spectra have been normalized to the transmission through straight photonic crystal waveguide of the same length to eliminate the coupling and the propagation loss in straight waveguides. Dashed line marks a bend loss of 1 dB.

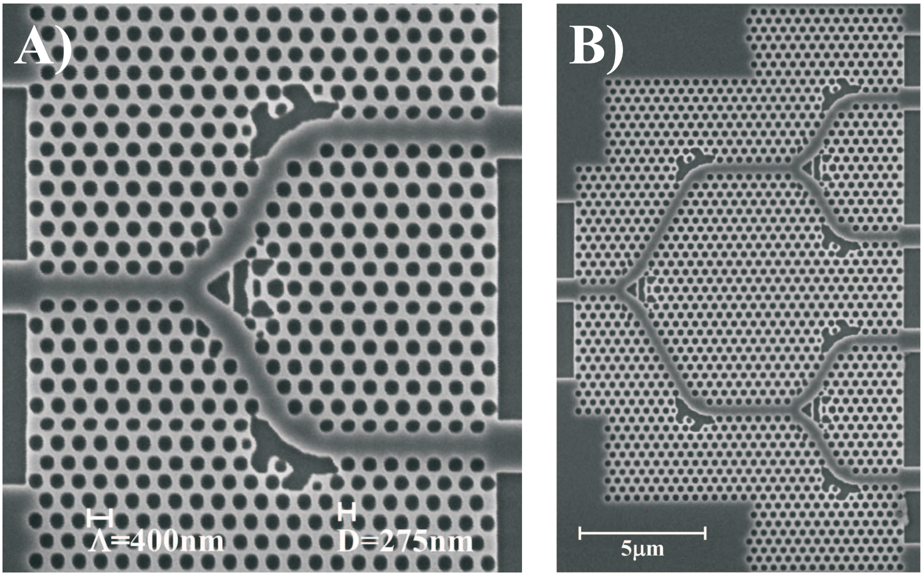

Figure 5.14: SEM images of the fabricated structures containing the topology optimized Y-junction and 60 bends. The pitch of the triangular lattice is $\Lambda =$ 400 nm with hole diameter $D = 275$ nm. A) 1×2-splitter. B) 1×4 splitter. The number, shape and size of the holes at each bend are designed using topology optimization

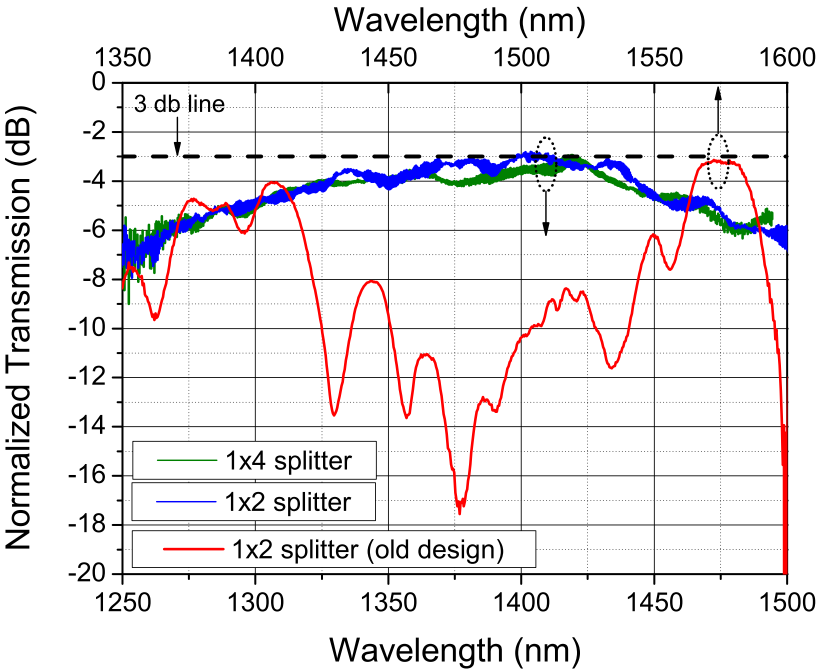

Figure 5.15: Measured transmission for the two output ports for the topology optimized component. Also shown is the measured normalized output from a previously fabricated splitter with consecutive 60 degree bends. For this component the wavelength range roughly corresponds to 1350-1600 nm. The dashed line at 3 dB corresponds to zero excess loss of the component.

Chapter 6

Conclusion

The work described in this thesis covered the issues of fabricating materials for use as base material for making photonic crystals and the design of photonic crystal components.

In the work regarding the material fabrication the aim was to investigate the possibilities to fabricate a silicon-on-insulator material using standard cleanroom processing techniques. A standard silicon wafer was covered with a $\sim$1.8 μm silica film by an oxidation process. Subsequently it was covered with a thin silicon layer deposited from silane by a LPCVD process. Such a process sequence is in principle rather straightforward and benefits from being much cheaper compared to acquiring commercial SOI substrates. The fabricated materials were evaluated by performing transmission measurements using a cut-back method on standard ridge waveguides formed in the deposited silicon film. The material properties of the LPCVD film depend strongly on the deposition temperature. The surface roughness of the deposited films was decreased by lowering the deposition temperature, this is important in order to reduce scattering. However this deposition temperature results in an amorphous structure reported to have a large intrinsic loss. To comply with this the film has been crystallized by annealing at temperatures of 800°C and 1100°C. To alter the interaction between the waveguide mode and the lossy waveguide core, several geometric investigations were carried out. This included making silicon films with different thicknesses ranging from 300 nm to 2.0 μm and covering the waveguides with a top cladding silica layer by a PECVD process. These investigations did however not result in any good material properties as the material loss was estimated to be >65–70 dB for waveguides having a length of 4 mm, and therefore not applicable for any practical purposes. The investigation was decided to be terminated at this point in order to focus on the actual photonic crystals instead. Investigations of more fundamental aspects of the fabricated silicon have not been carried out as this was not the main subject and because of limitations in time and the available equipment.

The other part of the work was concerned with design, fabrication and characterization of photonic crystal components. The performance of simple photonic crystals has been optimized using a design method adopted from mechanical engineering called topology optimization. This method has been employed for designing a photonic crystal z-bend. The z-bend shows a greatly improved performance when the topology optimization procedure is applied, as confirmed by numerical 3D FDTD simulations. The photonic crystal z-bend was subsequently fabricated utilizing e-beam lithography and reactive ions etch. Thereafter it was optically characterized, and it showed a very good performance having a very low bend loss of 1 dB in a wavelength range of more than 200 nm. This method has also been applied to other types of photonic crystals components with a similar excellent performance of the fabricated structures.

The above components are all characterized by displaying a low loss in a large bandwidth range. Functionalities such as the ones obtained in an add-drop filter have also been investigated using the topology optimizing method, but narrow bandwidth functionalities show some difficulties with the current implementation of the method. Therefore other methods were applied. The in-plane coupling between waveguides and a cavity was investigated using 2D FDTD simulations. The work performed so far on this subject shows some possibilities. However, until now only a qualitative analysis has been performed and further work is necessary in order to reach a design for a fully functional add-drop filter, and no firm conclusions on this point was obtained.

The expected importance of photonic crystal components as substitutes for the more conventional silicon strip waveguides have very recently been diminished. One of the biggest problems in fabricating strip waveguides in silicon is scattering from roughness due the fabrication process, which have a great impact due to the high index contrast, especially on waveguide bends. As the fabrication technologies are continuously being improved, research groups have demonstrated silicon strip waveguides showing propagation and, most importantly, bending loss characteristics approaching their photonic crystal counterparts. So for a use for point-to-point transmission the photonic crystal is seemingly not as superior as anticipated, and devices with a hybrid integration between photonic crystals and conventional strip waveguides have been suggested. However, photonic crystals still have some very unique optical properties. Very high Q-values and very small mode volumes of the defect modes in cavities have been reported. This is extremely important for active devices and expectingly it is probably within these research areas, together with narrow band filter applications, that photonic crystal will prove their superior usefulness in future ultra compact optical integrated circuits.

Appendix A

Publications

International Journals

1. J. S. Jensen, O. Sigmund, L. H. Frandsen, P. I. Borel, A. Harpøth, and M. Kristensen, *Topology Design and fabrication of a new double 90-degree photonic crystal waveguide bend*, Photon. Techn. Lett. **16** (6), 1202–1204 (2005)

2. P.I. Borel, L.H. Frandsen, A. Harpøth, M. Kristensen, J.S. Jensen and O. Sigmund, *Topology Optimised Broadband Photonic Crystal Y-Splitter*, Electron. Lett. **41** (2), 69–71 (2005).

3. L.H. Frandsen, A. Harpøth, P.I. Borel, M. Kristensen, J.S. Jensen and O. Sigmund *Broadband photonic crystal waveguide 60° bend obtained utilizing topology optimization*, Optics Express, **12** (24), 5916–5921 (2004).

4. P.F. Xing, P.I. Borel, L. H. Frandsen, A. Harpøth and M. Kristensen, *Optimization of Bandwidth in 60 deg. Photonic Crystal Waveguide Bends*, Optics Communications, 248, 179–184 (2005).

5. P.I. Borel, L.H. Frandsen, A. Harpøth, J.B. Leon, H. Liu, M. Kristensen, W. Bogaerts, P. Dumon, R. Baets, V. Wiaux, J. Wouters and S. Beckx *Bandwidth engineering of photonic crystal waveguide bends*, Electron. Lett. **40** (20), 1263–1265 (2004).

6. L.H. Frandsen, P.I. Borel, Y.X. Zhuang, A. Harpøth, M. Thorhauge, M. Kristensen, W. Bogaerts, P. Dumon, R. Baets, V. Wiaux, J. Wouters and S. Beckx, *Ultra-low-loss 3-dB Photonic Crystal Waveguide Splitter*, Optics Letters, **29** (14), 1623–1625 (2004).

7. P.I. Borel, A. Harpøth, L.H. Frandsen, M. Kristensen, P. Shi, J.S. Jensen and O. Sigmund, *Topology optimization and fabrication of photonic crystal structures*, Optics Express **12** (9), 1996–2001 (2004).

8. A. Lavrinenko, P.I. Borel, L.H. Frandsen, M. Thorhauge, A. Harpøth, M. Kristensen and T. Niemi, *Comprehensive FDTD Modelling of Photonic Crystal Waveguide Components*, Optics Express **12** (2), 234–248 (2004).

9. P.I. Borel, L.H. Frandsen, M. Thorhauge, A. Harpøth, Y.X. Zhuang, M. Kristensen and H.M.H Chong, *Efficient propagation of TM polarized light in photonic crystal components exhibiting band gaps for TE polarized light*, Optics Express **11** (15), 1757–1762 (2003).

International conference papers

Invited

1. P.I. Borel, L.H. Frandsen, A. Harpøth, T. Niemi and M. Kristensen, *Design and fabrication of SOI-based photonic crystal components*, Invited presentation at the ICTON/ESPC Conference, Wroclaw, Poland, July, 2004.

2. M. Kristensen, P.I. Borel, L.H. Frandsen, A. Harpøth and T. Niemi, *Design and Fabrication of Planar PBG Components*, Invited presentation at the EPS-QEOD Europhoton Conference on 'Solid-State and Fiber Coherent Light Sources', at EPFL, Switzerland, August, 2004.

Contributed

1. M. Kristensen, P.I. Borel, L.H. Frandsen, A. Harpøth, J.S. Jensen, and O. Sigmund *Optimized Planar Photonic Crystal Waveguide 60 Bend with more than 200nm Wide 1-dB Transmission Bandwidth*, **Paper WD6** OFC'05, Anaheim, California, March 6-11, 2005.

2. M. Thorhauge, L.H. Frandsen, P.I. Borel, A. Harpøth, Y.X. Zhuang, M. Kristensen, W. Bogaerts, P. Dumon, R. Baets, V. Wiaux, J. Wouters and S. Beckx, *Novel low-loss 60 bends in photonic crystal waveguides*, **paper CWP2**, 122, CLEO, San Francisco, California, USA, May 16-21, 2004.

3. A. Harpøth, L.H. Frandsen, M. Kristensen, P.I. Borel, J.S. Jensen, O. Sigmund and P. Shi, *Fabrication of topology optimized photonic crystal waveguide Z-bend displaying large bandwidth with very low bend loss*, **Paper Tu-E3**, 83, PECS-V, Kyoto, Japan, March 7-11, 2004.

4. M. Kristensen, L.H. Frandsen, A. Harpøth, Y.X. Zhuang, P.I. Borel, W. Bogaerts, P. Dumon, R. Baets, V. Wiaux, J. Wouters and S. Beckx, *Large bandwidth 60 bend in photonic crystal waveguides*, **Paper Tu-F5**, 93, PECS-V, Kyoto, Japan, March 7-11, 2004.
5. L.H. Frandsen, P.I. Borel, A. Harpøth, M. Kristensen, M. Thorhauge, W. Bogaerts, P. Dumon, R. Baets, V. Wiaux, J. Wouters and S. Beckx, *Ultra low loss photonic crystal waveguide 3 dB splitter*, **Paper Tu-P52**, 146, PECS-V, Kyoto, Japan, March 7-11, 2004.
6. Y.X. Zhuang, L.H. Frandsen, A. Harpøth, M. Thorhauge, M. Kristensen, P.I. Borel, W. Bogaerts and R. Baets, *Wavelength tuning of photonic crystal waveguides fabricated using 248-nm deep UV lithography*, **Paper ThR2**, OFC'04, Los Angeles, February 22-27, 2004.
7. L.H. Frandsen, M. Thorhauge, P.I. Borel, M. Kristensen, A. Harpøth, H.M.H. Chong and R.M. de la Rue, *Ultra-compact photonic bandgap waveguide coupler*, **Paper Tu1.1.4**, 5, 44-45, ECOC'03, Rimini, Italy, September 21-25, 2003.

Bibliography

[1] G. K. Celler and S. Cristoloveanu. Frontiers of silicon-on-insulator. *Appl. Phys. Rev.*, 93(9):4955–4978, 2003.

[2] S. M. Sze. *VLSI Technology*. McGRAW-HILL, second edition, 1988.

[3] E. Yablonovitch. Inhibited spontaneous emission in solid-state physics and electronics. *Phys. Rev. Lett.*, 58(20):2059–2062, 1987.

[4] S. John. Strong localization of photons in certain disordered dielectric super lattices. *Phys. Rev. Lett.*, 58(23):2486–2489, 1987.

[5] T. F. Krauss, R. M. De La Rue, and S. Brand. Two-dimensional photonic-bandgap structures operating at near-infrared wavelengths. *Nature*, 383(6602):699–702, 1996.

[6] S. G. Johnson, S. Fan, P. R. Villeneuve, and J. D. Joannopoulos. Guided modes in photonic crystal slabs. *Phys. Rev. B*, 60(8):5751–5758, 1999.

[7] S. J. McNab, N. Moll, and Y. A. Vlasov. Ultra-low loss photonic integrated circuits with membrane-type photonic crystal waveguides. *Optics Express*, 11(22):2927–2939, 2003.

[8] Y. Sugimoto, Y. Tanaka, N. Ikeda, T. Yang, H. Nakamura, K. Asakawa, K. Inoue, T. Maruyama, K. Miyashita, K. Ishida, and Y. Watanabe. Design, fabrication, and characterization of coupling strength-controlled directional coupler based on two-dimensional photonic-crystal slab waveguides. *Appl. Phys. Lett.*, 83(16):3236–3238, 2003.

[9] M. Notomi, A. Shinya, S. Mitsugi, E. Kuramochi, and H-Y. Ryu. Waveguides, resonators and their coupled elements in photonic crystal slabs. *Optics Express*, 12(8):1551–1561, 2004.

[10] B-S. Song, S. Noda, and T. Asano. Photonic devices based on in-plane hetero photonic crystals. *Science*, 300:1537, 2003.

[11] Y. Akahane, T. Asano, B-S. Song, and S. Noda. High-Q photonic nanocavity in a two-dimensional photonic crystal. *Nature*, 425:944–947, 2003.

[12] H-Y. Ryo, M. Notomi, and Y-H. Lee. High-quality-factor and small-mode-volume hexapole modes in photonic-crystal-slab nanocavities. *Appl. Phys. Lett.*, 83(21):4294–4296, 2003.

[13] P. I. Borel, A. Harpøth, L. H. Frandsen, M. Kristensen, P. Shi, J. S. Jensen, and O. Sigmund. Topology optimization of photonic crystal structures. *Optics Express*, 12(9):1996–2001, 2004.

[14] Kristian Rechendorff, Lars Hagedorn Frandsen, Peter Ingo Borel, and Erik Schon. Private communication.

[15] T. F. Kraus and R. M. De La Rue. Photonic crystals in the optical regime-past, present and future. *Prog. in Quant. Elec.*, 23:51–96, 1999.

[16] M. Olivier and J-C. Peuzin. Characterization of silicon layers via guided wave optics. *Appl. Phys. Lett.*, 32(6):386–388, 1978.

[17] R. A. Soref and J. P. Lorenzo. All-silicon active and passive guided-wave components for $\lambda = 1.3$ and 1.6 μm. *J. Quan. Elec.*, QE-22(6):873–879, 1986.

[18] R. A. Soref and J. P. Lorenzo. Silicon guided-wave optics. *Solid State Technology*, pages 95–98, November 1988.

[19] B. N. Kurdi and D. G. Hall. Optical waveguides in oxygen-implanted buried-oxide silicon-on-insulator structures. *Opt. Lett.*, 13(2):175–177, 1988.

[20] R. M. Emmons, B. N. Kurdi, and D. G. Hall. Buried-oxide Silicon-On-Insulator structures I: Optical waveguide characteristics. *J. Quant. Elec.*, 28(1):157–163, 1992.

[21] A. Rickman, G. T. Reed, B. L. Weiss, and F. Namavar. Low-loss planar optical waveguides fabricated in SIMOX material. *IEEE Phot. Tech. Lett.*, 4(6):633–635, 1992.

[22] K. K. Lee, D. R. Lim, and L. C. Kimerling. Fabrication of ultralow-loss Si/SiO_2 waveguides by roughness reduction. *Optics letters*, 26(23):1888–1890, 2001.

[23] K. K. Lee, D. R. Lim, H. Luan, A. Agarwal, J. Foresi, and L. C. Kimerling. Effect of size and roughness on light transmission in a Si/SiO_2 waveguide: Experiments and model. *Appl. Phys. Lett.*, 77(11):1617–1619, 2000.

[24] Leif S. Johansen. *Microelectronics for Micromechanics.* PhD thesis, MIC, technical University of Denmark, 2000.

[25] A. M. Agarwal, L. Liao, J. S. Foresi, M. R. Black, X. Duan, and L. C. Kimerling. Low-loss polycrystalline waveguides for silicon photonics. *J. Appl. Phys*, 80(11):6120–6123, 1996.

[26] W. B. Jackson, N. M. Johnson, and D. K. Biegelsen. Density of gap states of silicon grain boundaries determined by optical absorption. *Appl. Phys. Lett.*, 43(2):195–197, 1983.

[27] R. E. Jones and P. S. Wesolowski. Electrical, thermoelectric, and optical properties of strongly degenerate polycrystalline films. *J. Appl. Phys.*, 56(6):1701–1706, 1984.

[28] J. S. Foresi, M. R. Black, A. M. Agarwal, and L. C. Kimerling. Losses in polycrystalline silicon waveguides. *Appl. Phys. Lett.*, 68(15):2052–2054, 1996.

[29] A. M. Agarwal, M. R. Black, J. S. Foresi, L. Liao, Y. Liu, and L. C. Kimerling. Polysilicon waveguides for silicon photonics. *Mat. Res. Soc. Symp. Proc.*, vol 403:327–332, 1996.

[30] L. Liao, D. R. Lim, A. M. Agarwal, X. Duan, K. K. Lee, and L.C. Kimerling. Optical transmission losses in polycrystalline silicon strip waveguides: Effects of waveguide dimensions, thermal treatment, hydrogen passivation, and wavelength. *Journal of Electronic Materials*, vol. 29(12):1380–1386, 2000.

[31] Graham T. Reed and Andrew P. Knights. *Silicon Photonics, an Introduction.* WILEY, 2004.

[32] B. E. Deal and A. S. Grove. General relationship for the thermal oxidation of silicon. *J. Appl. Phys.*, 36(12):3770–3778, 1965.

[33] B. A. Scott, R. D. Estes, and J. M. Jasinski. The role of surface reactions in monosilane pyrolysis. *J. Chem. Phys.*, 89(4):2544–2549, 1988.

[34] B. A. Scott and R. D. Estes. Role of gas phase reactions in silicon chemical vapour deposition from monosilane. *Appl. Phys. Lett.*, 55(10):1005–1007, 1989.

[35] Milton Ohring. *The Materials Science of Thin Films.* ACADEMIC PRESS, 1992.

[36] Marc Madou. *Fundamentals of Microfabrication.* CRC Press LLC, 1997.

[37] M. Tao and L. P. Hunt. Crystal growth in silicon chemical vapor deposition from silane, the role of hydrogen. *J. Electrochem. Soc.*, 144(6):2221–2225, 1997.

[38] Peter Allen Krulevitch. *Micromechanical Investigations of Silicon and Ni-Ti-Cu Thin Films.* PhD thesis, University of California at Berkeley, 1994.

[39] A. M. Beers, H. T. J. M. Hintzen, and J. Bloem. Solid state transitions during the growth of silicon by chemical vapour deposition. *Solid State Chemistry 1982, Proceedings of the European Conference*, pages 177–180.

[40] Bo Asp Møller Andersen. *Fabrication Technologi for Fiber Terminated Planar Waveguide Components.* PhD thesis, MIC, technical University of Denmark, 1997.

[41] Robert G. Hunsberger. *Integrated Optics, Theory and Technology.* Springer, fourth edition, 1995.

[42] D. Marcuse. Mode conversion caused by surface imperfections of a dielectric slab waveguide. *The Bell System Technical Journal*, pages 3187–3215, December 1969.

[43] P. K. Tien. Light waves in thin films and integrated optics. *Appl. Opt.*, 10(11):2395–2413, 1971.

[44] J. P. R. Lacey and F. P. Payne. Radiation loss from planar waveguides with random wall imperfections. *IEE Proceedings*, 137(4):282–288, 1990.

[45] P. F. Payne and J. P. R. Lacey. A theoretical analysis of scattering loss from planar optical waveguides. *optical and Quantum electronics*, 26:977–986, 1994.

[46] F. Ladouceur, J. D. Love, and T. J. Senden. Effect of side wall roughness in buried channel waveguides. *IEE Proc.-Optoelectron.*, 141(4):242–248, 1994.

[47] Francois Ladouceur and John D. Love. *Silica-Based Buried Channel Waveguides and Devices.* CHAPMANN & HALL, 1996.

[48] F. Ladouceur, J. D. Love, and T. J. Senden. Measurement of surface roughness in buried channel waveguides. *Electron. Lett.*, 28(14):1321–1322, 1992.

[49] A. Säynätjoki, J. Riikonen, and H. Lipsanen. Optical waveguides on polysilicon-on-insulator. *J. Mat. Sci.: Mat. in Elec.*, 14:417–420, 2003.

[50] L. Lai and E. A. Irene. Limiting Si/SiO_2 interface roughness resulting from thermal oxidation. *J. Appl. Phys.*, 86(3):1729–1735, 1999.

[51] A. Lavrinenko, P. I. Borel, L. H. Frandsen, M. Thorhauge, A. Harpøth, M. Kristensen, T. Niemi, and H. M. H. Chong. Comprehensive FDTD modelling of photonic crystal waveguide components. *Optics Express*, 12(2):234–248, 2004.

[52] J. D. Jackson. *Classical Electrodynamics*. Wiley, New York, 1962.

[53] John D. Joannopoulos, Robert D. Meade, and Joshua N. Winn. *Photonic Crystals, Molding the Flow of Light*. Princeton University Press, 1995.

[54] S. Guo. Plane wave expansion method for photonic band gap, calculation using MATLAB.
http://www.lions.odu.edu/∼sguox002/pbgweb/pwmmanual.pdf.

[55] S. G. Johnson and J. D. Joannopoulos. The MIT Photonic-Bands package home page.
http://ab-initio.mit.edu/mpb/.

[56] R. D. Meade, A. M. Rappe, K. D. Brommer, J. D. Joannopoulos, and O. L. Alerhand. Accurate theoretical analysis of photonic band-gap materials. *Phys. Rev. B*, 48(11):8434–8437, 1993.

[57] S. G. Johnson and J. D. Joannopoulos. Block-iterative frequency-domain methods for maxwell's equation in a planewave basis. *Optics Express*, 8(3):173–190, 2001.

[58] Charles Kittel. *Introduction to Solid State Physics*. Wiley, seventh edition, 1996.

[59] O. Painter, J. Vučković, and A. Scherer. Defect modes of a two-dimensional photonic crystal in an optically thin dielectric slab. *J. Opt. Soc. Am. B*, 16(2):275–285, 1999.

[60] C. Jamois, R. B. Wehrspohn, L. C. Andreani, C. Hermann, O. Hess, and U. Gösele. Silicon-based two-dimensional photonic crystal waveguides. *Photonics and nanostructure, Fundamentals and Applications*, 1:1–13, 1003.

[61] Thomas Søndergaard. *Optics of Dielectric Structures*. PhD thesis, Research Center COM, Technical University of Denmark, 2002.

[62] S. G. Johnson, P. R. Villeneuve, S. Fan, and J. D. Joannopoulos. Linear waveguides in photonic-crystal slabs. *Phys. Rev. B*, 62(12):8212–8222, 2000.

[63] Allen Taflove. *Advances in Computational Electrodynamics, The Finite Difference Time Domain Method*. Artech House Publishers, 1998.

[64] A. J. Ward and J. B. Pendry. A program for calculating photonic band structures and green's functions using a non-orthogonal FDTD method. *Comp. Phys. Comm.*, 122:23–41, 1998.

[65] A. J. Ward and J. B. Pendry. Refraction and geometry in maxwell's equations. *J. Mod. Opt.*, 43(4):773–793, 1996.

[66] *Crystal wave*-manual.

[67] A. J. Ward and J. B. Pendry. A programme for calculating photonic band structures and green's functions using a non-orthogonal FDTD method. *Comp. Phys. Com.*, 112:23–41, 1998.

[68] A. Chutinan, M. Okano, and S. Noda. Wider bandwidth with high transmission through waveguide bends in two-dimensional photonic crystal slabs. *Appl .Phys. Lett.*, 80(10):1698–1700, 2002.

[69] A. Talneau, L. Le Gouezigou, N. Bouadma, M. Kafesaki, C. M. Soukolis, and M. Agio. Photonic-crystal ultrashort bends with improved transmission and low reflection at 1.55 μm. *Appl. Phys. Lett.*, 80(4):547–549, 2002.

[70] S. Boscolo, M. Midrio, and T. F. Krauss. Y-junctions in photonic crystal channel waveguides: High transmission and impedance matching. *Opt. Lett.*, 27(12):1001–1003, 2002.

[71] R. Wilson, T. J. Karle, I. Moerman, and T. J. Krauss. Efficient photonic crystal Y-junction. *J. Opt. A: Pure Appl. Opt.*, 5:S76–S80, 2003.

[72] L. H. Frandsen, P. I. Borel, Y. X. Zhuang, A. Harpøth, M. Thorhauge, M. Kristensen, W. Bogaerts, P. Dumon, R. Baets, J. Wiaux, and S. Beckx. Ultralow-loss 3-dB photonic crystal splitter. *Opt. Lett.*, 29(14):1623, 2004.

[73] M. Thorhauge, L. H. Frandsen, and P. I. Borel. Efficient photonic crystal directional couplers. *Opt. Lett.*, 28(17):1525, 2003.

[74] E. Yablonovitch. Inverse design of dielectric and plasmonic crystals. *Technical Digest: International Symposium on Photonic Crystals and Electromagnetic Structures V (PECS-V)*, paper Tu-D1:73, 7.–11. March, Kyoto 2004.

[75] M. Burger, S. J. Osher, and E. Yablonovitch. Inverse problem techniques for the design of photonic crystals. *IEICE Transactions on Electronics*, E87-C(3):258–265, 2004.

[76] S. J. Cox and D. C. Dobson. Band structure optimization of two-dimensional photonic crystal in H-polarization. *J. Comp. Phys.*, 158:214–224, 2000.

[77] C. D. Dobson and F. Santosa. Optimal localization of eigenfunctions in an inhomogeneous medium. *SIAM J. Appl. Math.*, 64(3):762–774, 2004.

[78] O. Sigmund and J. Jensen. Systematic design of phononic band-gap materials and structures by topology optimization. *Phil. Trans. R. Soc. Lond. A*, 361:1001–1019, 2003.

[79] O. Sigmund. Topology optimization: A tool for the tailoring of structures and materials. *Phil. Trans. R. Soc. Lond. A*, 358:211–227, 2000.

[80] M. P. Bendsøe and O. Sigmund. *Topology Optimization.* Springer, second edition, 2003.

[81] J. S. Jensen and O. Sigmund. Systematic design of photonic crystal structures using topology optimization: Low-loss waveguide bends. *Appl. Phys. Lett.*, 84(12):2022–2024, 2004.

[82] J. S. Jensen and O. Sigmund. Topology optimization of photonic crystal structures: A high bandwidth low loss T-junction waveguide. *J. Opt. Soc. Am. B*, 22(6):1191–1198, 2005.

[83] R. D. Cook, M. E. Malkus, D. S. Plesha, and R. J. Witt. *Concepts and Application of Finite Element Analysis.* Wiley, New York, 4. edition, 2002.

[84] K. Svanberg. The method of moving asymptotes - a new method for structural optimization. *Int. Numer. Methods Eng.*, 24:359–373, 1987.

[85] E. Yablonovitch, T. J. Gmitter, R. D. Meade, A. M. Rappe, K. D. Brommer, and J. D. Joannopoulos. Donor and acceptor modes in photonic bandgap structure. *Phys. Rev. Lett.*, 67(24):3380–3383, 1991.

[86] A. Chutinan, M. Mochizuki, M. Imada, and S. Noda. Surface-emitting channel drop filters using single defects in two-dimensional photonic crystal slabs. *Appl. Phys. lett.*, 79(17):2690–2692, 2001.

[87] S. Noda, A. Chutinan, and M. Imada. Trapping and emission of photons by a single defect in a photonic bandgap structure. *Nature*, 407:608–610, 2000.

[88] Y. Akahane, M. Mochizuki, T. Asano, Y. Tanaka, and S. Noda. Design of a channel drop filter by using a donor-type cavity with a high quality factor in a two-dimensional photonic crystal slab. *Appl. Phys. Lett.*, 82(9):1341–1343, 2003.

[89] Y. Akahane, T. Asano, B-S. Song, and S. Noda. Investigation of high-Q channel drop filters using donor-type defects in two-dimensional photonic crystal slabs. *App. Phys. Lett.*, 83(8):1525–1514, 2003.

[90] K. Srinivasan and O. Painter. Momentum space design of high-Q photonic crystal optical waveguides. *Optics Express*, 10(15):670–684, 2002.

[91] J. Vučković, M. Lončar, H. Mabuchi, and A. Scherer. Optimization of the Q-factor in photonic crystal microcavities. *J. Quant. Elec.*, 38(7):850–856, 2002.

[92] H. Takano, Y. Akahane, T. Asano, and S. Noda. In-plane-type channel drop filter in a two-dimensional photonic crystal slab. *App. Phys. Lett.*, 84(13):2226–2228, 2004.

[93] S. Fan, J. N. Winn, A. Devenyi, J. C. Chen, R. D. Meade, and J. D. Joannopoulos. Guided and defect modes in periodic dielectric waveguides. *J. Opt. Soc. Am. B*, 12(7):1267–1272, 1995.

[94] S. Guo and S. Albin. Numerical techniques for excitation and analysis of defect modes in photonic crystals. *Optics Express*, 11(9):1080–1089, 2003.

[95] S. Fan, P. R. Villeneuve, J. D. Joannopoulos, and H. A. Haus. Channel drop tunneling through localized states. *Phys. Rev. Lett.*, 80:960–963, 1998.

[96] J. M. Jouanno, D. Zauner, and M. Kristensen. Low crosstalk planar optical add-drop multiplexer fabricated with UV-induced bragg gratings. *Elec. Lett.*, 33(25):2120–2121, 1997.

[97] W. Bogaerts, V. Wiaux, D. Taillaert, S. Beckx, B. Luyssaert, P. Bienstman, and R. Baets. Fabrication of photonic crystals in silicon-on-insulator using 248-nm deep UV lithography. *IEEE J. Sel. Top. Quantum Electron.*, 8:928–934, 2002.

[98] W. Bogaerts, V. Wiaux, P. Dumon, D. Taillert, J. Wouters, S. Beckx, J. Van Campenhout, B. Luyssaert, and R. Baets. Large-scale production techniques for photonic nanostructures. *Proc. SPIE*, 5225:101–112, 2003.

[99] Kristján Leósson. *Optical Properties of Localized Excitons in Semiconductor Nanostructures.* PhD thesis, Research Center COM, Technical University of Denmark, 2001.

[100] Jesper Arentoft Jayaswal, Alexandra Boltasseva, Jesper Bo Damm Jensen, Peter Ingo Borel, and Lars Hagedorn Frandsen. *Fabrication and Characterization of SOI Based Photonic Crystal Waveguides & Components at COM.* Research Center COM, Technical University of Denmark, May 2002.

[101] P. Rai-Choudhuri. *Handbook of Microlithography, Micromachining, and Microfabrication*, volume 1. SPIE Press, 1997. http://www.cnf.cornell.edu/spiebook/TOC.HTM.

[102] Dan Zauner. *Integrated Optical Devices for Wavelength Division Multiplexing Using PECVD and Direct UV-Writing Techniques.* PhD thesis, Research Center COM, Technical University of Denmark, 2000.

[103] B. A. M. Andersen, O. Hansen, and M. Kristensen. Spatial variation of the etch rate for deep etching of silicon by reactive ion etching. *J. Vac. Sci. Technol. B*, 15(4):993–999, 1997.

[104] Ole Hansen. Private communication.

[105] Lars Hagedorn Frandsen. Fabrication and characterization of PBG waveguide components. Master's thesis, Research Center COM, Technical University of Denmark, 2003.

[106] P. I. Borel, L. H. Frandsen, M. Thorhauge, A. Harpøth, Y. X. Zhuang, M. Kristensen, and H. M. H. Chong. Efficient propagation of TM polarized light in photonic crystal components exhibiting band gaps for TE polarized light. *Optics Express*, 11(15):1757–1762, 2003.

[107] L. H. Frandsen, A. Harpøth, P. I. Borel, M. Kristensen, J. S. Jensen, and O. Sigmund. Broadband photonic crystal waveguide 60° bend obtained utilizing topology optimization. *Optics Express*, 12(24):5916–5921, 2004.

[108] P. I. Borel, L. H. Frandsen, A. Harpøth, M. Kristensen, J. S. Jensen, and O. Sigmund. Topology optimised broadband photonic crystal y-splitter. *Electron. Lett.*, 41(2):69–71, 2005.

[109] J. S. Jensen, O. Sigmund, L. H. Frandsen, P. I. Borel, A. Harpøth, and M. Kristensen. Topology design and fabrication of a new double 90-degree photonic crystal waveguide bend. *Photon. Techn. Lett.*, 17(6):1202–1204, 2005.